Probing the Nature of Young Puffy Planets Through Theoretical Mass Constraints

Amalia Karalis

Supervised by Prof. Eve J. Lee

Department of Physics

McGill University

Montréal, Québec, Canada

April 15, 2024

A thesis submitted to McGill University in partial fulfillment of the requirements of the degree of Masters of Science

Abstract

Discoveries of close-in young puffy ($R_p \gtrsim 6\ R_\oplus$) planets raise the question of whether they are bonafide hot Jupiters or puffed-up Neptunes, potentially placing constraints on the formation location and timescale of hot Jupiters. Obtaining mass measurements for these planets is challenging due to stellar activity and noisy spectra. Therefore, we aim to provide independent theoretical constraints on the masses of these young planets based on their radii, incident fluxes, and ages, benchmarking to the planets of age <1 Gyr detected by K2 and TESS. Through a combination of interior structure models, considerations of photoevaporative mass loss, and empirical mass-metallicity trends, we present the range of possible masses for ∼26 planets of age ∼5-900 Myr and radii ∼3-16 $R_\oplus$. We find that for the candidate hot Jupiters ($R_p \gtrsim 6R_\oplus$), planets with radii $\lesssim 9R_\oplus$ are found to be below the gas giant planet mass regime ($\lesssim 100\ M_\oplus$), while for planets with $R_p \gtrsim 9R_\oplus$, we cannot rule out the possibility of them being gas giants. We further find that stellar metallicity is an important constraint on the upper limit of the mass, and we emphasize the importance of refining stellar abundances for young planet-hosting stars. Given our data and our results, all the youngest planets ($\lesssim$ 100 Myr) are likely puffed-up, Neptune-mass planets, while the bonafide hot Jupiters are only found around stars aged at least a few hundred Myr. This implies that high eccentricity tidal migration, which operates over timescales of hundreds of Myr to Gyr, is likely the dominant origin channel for hot Jupiters.

Abrégé

La découverte de jeunes planètes gonflées ($R_p \gtrsim 6$ $R_\oplus$) proches de leurs étoiles pose la question de savoir s'il s'agit de véritables Jupiters chaudes ou de Neptunes gonflées, ce qui pourrait imposer des contraintes sur le lieu et l'échelle de temps de formation des Jupiters chaudes. Obtenir des mesures de masse pour ces planètes est un défi en raison de l'activité stellaire et des spectres bruyants des jeunes étoiles hôtes. Par conséquent, nous visons à fournir des contraintes théoriques indépendantes sur les masses de ces jeunes planètes en nous basant sur leurs rayons, leurs flux incidents et leurs âges, en les comparant aux planètes d'âge <1 Gyr détectées par K2 et TESS. En combinant des modèles de structure intérieure, des considérations sur la perte de masse par photoévaporation et des tendances empiriques de masse-métallicité, nous présentons l'intervalle de masses possibles pour ∼26 planètes d'âge ∼5-900 Myr et de rayons ∼3-16 $R_\oplus$. Nous trouvons que pour les Jupiters chaudes candidates ($R_p \gtrsim 6R_\oplus$), les planètes de rayon $\lesssim 9R_\oplus$ sont en dessous du régime de masse des planètes géantes ($\lesssim 100$ $M_\oplus$), alors que pour les planètes de $R_p \gtrsim 9R_\oplus$, nous ne pouvons pas exclure la possibilité qu'elles soient des géantes. Nous constatons également que la métallicité stellaire est une contrainte importante sur la limite supérieure de la masse et nous soulignons l'importance du suivi des abondances stellaires pour les jeunes étoiles hôtes. Compte tenu de nos données et de nos résultats, toutes les planètes les plus jeunes ($\lesssim$ 100 Myr) sont probablement des planètes gonflées de la masse de Neptune, tandis que les véritables Jupiters chaudes ne se trouvent qu'autour d'étoiles âgées d'au moins quelques centaines de Myr. Cela implique que la migration des marées à haute excentricité, qui opère sur des échelles de temps allant de centaines de Myr à Gyr, est probablement le canal d'origine dominant pour les Jupiters chaudes.

Acknowledgements

First, I would like to express my gratitude to Professor Eve J. Lee for her expertise, guidance and mentorship during my time at McGill. Her insightful feedback, patience and willingness to chat with me whenever I had questions have been instrumental in shaping the direction and quality of my research. Secondly, to my parents, for their unwavering support and for always encouraging and believing in me. You always pushed me to be independent and capable of pursuing anything I dreamed of. Third, to my friends, who have been with me through this entire degree. Rose Tereso, Alicia Lepitre, and Corinne Gauthier, for being there through it all, always cheering me on and believing in me. Nicole Ford, for the nights spent baking and talking. Laura Gonzalez Escudero, for the pick-me-ups, the laughs, and your support through all of this. Nayyer Raza, for all the long conversations and genuine advice. Tim Hallatt, for the city walks and the lunchtime chats. To the basement dwellers (Alice Curtin, Ketan Sand, Vishwangi Shah), and my fellow dungeon inhabitants (Sam Wong, Magnus L'Argent, Amanda Cook), for the company, the well-needed coffee and lunch breaks, and for your constant support and encouragement. And to my group (Maya Tatarelli, Vincent

Savignac, Kevin Marimbu) for your friendship, and for always lifting me up and cheering me on. And lastly, to Professor Adrian Liu, for all the leftover lunches and sweet treats, which were indispensable fuel for research and thesis writing.

This research has made use of the NASA Exoplanet Archive, which is operated by the California Institute of Technology, under contract with the National Aeronautics and Space Administration under the Exoplanet Exploration Program.

Contribution of Authors

Professor Eve J. Lee conceived the project. All calculations and computations were done by Amalia Karalis, under the supervision and direction of Professor Lee. Amalia Karalis wrote the majority of the thesis, under the guidance of Professor Lee, who reviewed and approved each chapter.

Contents

List of Figures

List of Tables

List of Acronyms

EUV Extreme Ultraviolet.

FISM Flare Irradiance Spectrum Model.

GCR Gas-to-Core mass Ratio.

MESA Modules for Experiment in Stellar Astrophysics.

MIST MESA Isochromes & Stellar Tracks.

TESS Transiting Exoplanet Survey Sattelite.

Chapter 1

Introduction

Theories explaining the origins of hot Jupiters, gas giants (M_p ~100 $M_\oplus$) with short orbital periods ($\lesssim$ 10 days), propose various mechanisms for the presence of such massive planets so close to their host stars (see Dawson & Johnson, 2018, for a review on the origins of hot Jupiters). It is unlikely that short period giants formed at their present-day orbits, which suggests that some migration mechanism must be responsible for the existence of these planets. There are two main proposed migration mechanisms for hot Jupiters. The theory of gas disk migration postulates that torques from the disk gas cause the giant planet to lose angular momentum, which drives the inwards migration (Lin & Papaloizou, 1979). On the other hand, high-eccentricity tidal migration theories propose that the gas giant is perturbed into a highly eccentric orbit, and tidal forces from the star on the planet circularize the orbit, decreasing the orbital distance (Ford et al., 2000; Wu & Murray, 2003). The former process can take place while the star is still young, on timescales of a few Myr (see, e.g., Mamajek, 2009; Michel et al., 2021, for disk gas dissipation timescales), while the latter occurs on a much longer timescale of a few hundred Myr to Gyr (see, e.g., Naoz et al., 2011; Petrovich, 2015, for dynamical simulations of high eccentricity tidal migration).

Discoveries of a population of young (<1 Gyr), Jupiter-sized ($R \gtrsim 6 R_\oplus$) planets at close-in orbits via transit from Kepler/K2 (Howell et al., 2014) and the Transiting Exoplanet Survey Satellite (TESS) (Ricker et al., 2015) indicate the existence of a group of candidate young hot Jupiters. However, young planets can sometimes appear inflated, as remnant heat from formation puffs up their atmospheres which have not yet cooled and settled onto their rocky cores, so this young population could also be made up of lower-mass planets with expanded atmospheres. This raises the question of whether this population of young, close-in planets consists of bonafide hot Jupiters or lighter, puffed-up Neptunes. Mass estimates for these puffy planets would indicate whether close-in gas giants can be found around young stars, which could potentially constrain the formation location and timescale of hot Jupiters.

In this thesis, we study a population of 26 transiting planets of age ∼5–900 Myr and radii ∼3–16 $R_\oplus$. To understand whether they are massive hot Jupiters or lighter, puffed-up Neptunes, we provide theoretical constraints on the masses of these young planets based on their radii, incident fluxes, and ages, using planetary interior structure models, considerations of photoevaporative mass loss, and empirical mass-metallicity trends. Our results will address whether hot Jupiters can be found close to their stars at young ages.

Chapter 2

Literature Review

The discovery of the first exoplanet orbiting a Sun-like star, 51 Pegasi b (Mayor & Queloz, 1995), launched a new era of innovation in the field of planetary science. This gas giant was unlike any of the planets in our solar system, with a mass almost 150 times that of the Earth and an orbit 8 times closer than Mercury's. Now known as hot Jupiters, these planets are gas giants with masses larger than $\sim$100 Earth masses and orbital periods shorter than 10 days (incident flux $\sim 1.72 \times 10^8$ erg/s/cm^2 if orbiting a Sun-like star). The existence of these hot giants presented a new challenge for planet formation theory: how could such a massive planet have formed so close to its star?

2.1 Planet Formation

Solid rocky cores form in a disk of gas and dust, growing in size as their orbital paths cross and they collide, merging to form a larger core. Although cores can begin to accrete their gaseous envelopes before these final mergers occur, large amounts of such accreted gas can be lost during collisions, depending on the angle and the velocity of the impact (e.g., Inamdar & Schlichting, 2016). Additionally, gas accretion rates increase with core mass (e.g., Lee & Chiang, 2015). Therefore, most of a planet's gaseous envelope is accreted following the core's final merger.

2.1.1 Gas Giant Planet Formation

A planet's rocky core accretes within its gravitational sphere of influence, the extent of which is set by the minimum of the Bondi (Bondi, 1952) and Hill (Hill, 1878) radii. The Bondi sphere is defined by the radius within which the escape velocity from the planet is less than the speed of sound,

$$R_{Bondi} = \frac{2GM_p}{c_s^2} \tag{2.1}$$

where G is the gravitational constant, M_p is the planet mass, and c_s is the speed of sound in the surrounding medium. For close-in planets where the stellar gravitational effects cannot be neglected, the accretion sphere is set by the Hill radius, defined as the radius where the tidal acceleration from the star balances the gravitational acceleration of the planet,

$$R_{Hill} = a\left(\frac{M_p}{3M_*}\right)^{1/3} \tag{2.2}$$

with a being the planet's semi-major axis and M_* being the host star's mass.

Gas accretion can be limited by thermodynamic cooling or hydrodynamic delivery. As the core begins to accrete gas, it is limited by the cooling time of the gas as it radiates away heat through the atmosphere. This radiative loss of heat allows the envelope to contract, freeing up space within the planet's accretion sphere.

Gas giant planets are believed to form via core-nucleated instability, a process by which a large, solid core embedded in the disk undergoes unstable gas accretion. This runaway gas accretion occurs for cores with masses above a critical value, typically around 10 $M_\oplus$ (see, e.g., Lee et al., 2014; Piso et al., 2015), depending on the opacity of the disk (Ikoma et al., 2000). This accelerated accretion is triggered when the self-gravity of the gaseous envelope becomes significant (when $M_{env} \sim M_{core}$). To maintain hydrostatic equilibrium as it accumulates large amounts of gas, the planet's luminosity increases to support the massive gaseous envelope against gravitational collapse. As heat is radiated away progressively more rapidly through the atmosphere, the cooling time shortens drastically. At this point, the planet enters the runaway state and accretion is limited by hydrodynamic delivery rather than cooling time (e.g., Pollack et al., 1996). This process results in the formation of gas giants, with final masses 100s of times that of the Earth.

2.1.2 Post-formation Cooling

A planet's thermal evolution post-formation (and after disk gas dissipation) is important in understanding how its radius changes, particularly at early times ($\lesssim$ Gyr). A planet's gaseous envelope can be treated as an adiabat, with cooling driven by the radiative transfer of heat through the atmosphere (see, e.g., Lopez & Fortney, 2014). As the atmosphere cools, the thermal pressure support decreases, resulting in the contraction of the atmosphere.

2.2 Photoevaporative Mass Loss

Once the planet has formed and the disk gas has dissipated, the planet's envelope is susceptible to mass loss through photoevaporation. Close-in planets are heavily irradiated by their host stars, and the influx of heat creates a thermal pressure gradient which counters the planet's gravitational potential, driving the outflow of gas. The rate at which mass is lost can be derived by equating the energy from high-energy XUV (X-ray and Extreme Ultraviolet, EUV) photons to the gravitational potential:

$$f_{XUV}\ \pi R_p^2 \cdot t = \frac{G M_p m_{gas}}{R_p} \tag{2.3}$$

$$\dot{m}_{gas} = -\frac{f_{XUV} R_p^3}{G M_p} \tag{2.4}$$

where f_{XUV} is the XUV flux on the planet from the host star, G is the gravitational constant, M_p is the planet mass, R_p is the planet radius, and $\dot{m}_{gas} = m_{gas}/t$ is the mass loss rate, for which we introduce a negative in the equation to express the loss of mass. Equation 2.4 describes the simplest approximation for energy-limited mass loss to which we gradually introduce corrections for the effects of the host star's gravity and mass loss efficiency.

In the simple approximation for the mass loss rate presented in Equation 2.4, the gravitational potential that the gas must overcome for escape to occur is simply that of the planet in isolation. However, the stellar gravitational field has a non-negligible effect on evaporation efficiency since it effectively decreases the gravitational binding energy of the planet's atmosphere. Erkaev et al. (2007) introduce a reduction factor, K, which accounts for the increased mass loss rate from the gravitational effects of the host star:

$$K = 1 - \frac{3}{2}\left(\frac{R_{Hill}}{R_p}\right)^{-1} + \frac{1}{2}\left(\frac{R_{Hill}}{R_p}\right)^{-3} \tag{2.5}$$

where R_{Hill} is the Hill radius, defined in Equation 2.2. As the gas expands, it spills out of the Roche Lobe radius of the planet, escaping as it overcomes the Roche Lobe potential.

Additional corrections to the mass loss rate are required to account for radiative losses (most prominently, the ionization of the hydrogen in the planetary atmosphere and metal line cooling), which contribute to lowering the efficiency of atmospheric escape since only a fraction of the stellar energy goes directly into heating the gas. As a result, the flux of escaping particles is limited by the amount of energy absorbed. This regime of mass-loss is referred to as energy-limited, first introduced by Watson et al. (1981), and incorporates an efficiency parameter, η, to the mass loss rate to account for this evaporation efficiency. The typical approach to energy-limited mass loss takes the efficiency to be a constant, usually between 0.1 and 1 (e.g. Lecavelier Des Etangs, 2007; Odert et al., 2020). This has been shown to overestimate the mass loss rate by several orders of magnitude (e.g., Owen & Jackson, 2012). For instance, Murray-Clay et al. (2009) find that the energy-limited approach breaks down for EUV fluxes $\gtrsim 10^4$ erg/s/cm^2, noting that the efficiency decreases with flux. In addition, Salz et al. (2016) investigated the role of the planet's gravitational potential, finding that the efficiency declines sharply with increasing potential (up to a potential of 13.1 erg/g). As a result, Caldiroli et al. (2022) develop an expression of the mass loss efficiency which evolves with flux and gravitational potential and present an equation for photoevaporative mass loss which encompasses both the energy-limited and the non-energy-limited regimes:

$$\dot{m}_{gas} = -\eta(f_{XUV}, R_p, M_p)\frac{\pi R_p^3 f_{XUV}}{GKM_p} \tag{2.6}$$

where $\eta(f_{XUV}, R_p, M_p)$ is the efficiency parameter obtained from empirical fitting to numerical simulations computed in Appendix A of Caldiroli et al. (2022).

2.3 Hot Jupiter Formation Mechanisms

There are three proposed formation mechanisms for hot Jupiters, illustrated in Figure 2.1. In situ formation postulates that the entire formation process of the Jupiter-sized planet would occur close to where it is observed (Batygin et al., 2015). Forming such a large planet first requires the coagulation of enough solids to form a core of at least $\sim$10 $M_\oplus$ (see, e.g., Lee et al., 2014; Piso et al., 2015) before disk gas dissipation so that runaway gas accretion occurs and puffs up the planet to Jupiter size. While core growth timescales are very short for planets within $\sim$ 0.1 AU, small feedings zones (zone within the disk where the growing core can gravitationally capture solids) and low surface densities limit the maximum core size (see Section 2.1 of Dawson & Johnson, 2018, and references therein, for a review on in situ formation of hot Jupiters). It is therefore unlikely that hot Jupiters form close-in.

The other two theories propose that the planet forms at much larger distances and then migrates close to its host star. In the theory of gas disk migration, torques from the disk gas cause the gas giant to migrate to shorter orbital distances. Perturbations caused by the gravitational potential of the planet excite waves within the gaseous disk. Lindblad resonance occurs where the oscillation time of the planet's perturbation (the forcing frequency) is comparable to the natural frequency of the disk gas (since gas parcels travel at sub-Keplerian speed, their orbital frequency is a combination of the epicyclic frequency and the frequency of sound waves) (Lin & Papaloizou, 1979). The net angular momentum on the planet is the sum of the torques from the gas, which are maximized at the resonant locations within the disk. At each resonance location, the net torque depends on the amount of gas present and the strength of the resonance. Typically, in a viscous disk, the pressure gradient force which causes the gas to travel at sub-Keplerian speeds shifts the resonance locations inwards (Ward, 1997; Papaloizou et al., 2007). As a result, the resonance locations outside the planet's orbit lie closer to the planet than the inner resonance locations, so the net torque is outwards, driving the inwards migration of the planet. This process is known as Type 1 migration and occurs for smaller planets not massive enough to significantly alter the structure of the disk. Gas giants, on the other hand, can be massive enough to carve out a gap in the disk. In this case, it is expected that the planet moves with the disk, undergoing Type 2 migration (Lin & Papaloizou, 1986), which leads to inwards migration for a planet in the inner region of a viscous accretion disk (see Chapter 7.1 of Armitage, 2013, for a full overview of planetary migration mechanisms in gaseous disks). Disk gas migration halts when the gas in the disk dissipates, over timescales of a few Myr (see, e.g., Mamajek, 2009; Michel et al., 2021).

High-eccentricity tidal migration theories instead propose that a perturbation by another object excites the gas giant into a highly elliptical orbit (Wu & Murray, 2003). Due to the extreme eccentricity of the orbit, the host star exerts large tidal forces on the planet when it is at closest approach (pericenter). This tidal dissipation causes the planet to lose orbital energy, damping the eccentricity and circularizing the gas giant's orbit. Over time, as the planet's orbit circularizes, the orbital distance decreases as the gas giant migrates closer to its host star, to short-period orbits within ~ 10 days (see Dawson & Johnson, 2018, for a full review of hot Jupiter formation mechanisms, including high eccentricity tidal migration). High eccentricity tidal migration occurs over Myr to Gyr timescales (see, e.g., dynamical simulations from Naoz et al., 2011; Petrovich, 2015).

The detection of young (< 1 Gyr), puffy ($R \gtrsim 6$ $R_\oplus$) planets from TESS and Kepler/K2 indicates the existence of a candidate population of Jupiter-sized planets. However, given their young age, it is also possible for these planets to be puffed-up Neptunes whose atmospheres have not yet cooled and settled onto their rocky cores. If these are bonafide hot Jupiters, their presence around young stars would imply the existence of a migration mechanism that operates over short (Myr) timescales. If they are instead Neptune mass, this indicates that hot Jupiters migrate over longer (Gyr) timescales and hence are unlikely to be found around young stars.

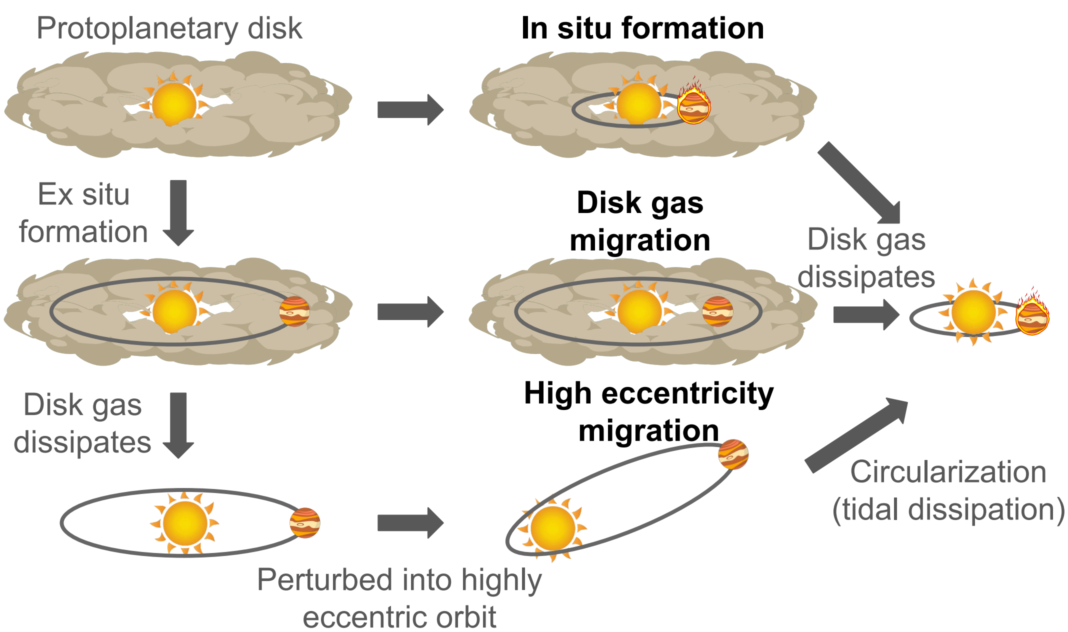

Figure 2.1: The three proposed formation mechanisms for hot Jupiters. In situ formation and disk gas migration occur over Myr timescales, on the order of the gas disk lifetime, while high eccentricity migration occurs over longer Myr to Gyr timescales, after the disk has dissipated.

Chapter 3

Methods

Our goal is to constrain the masses of the observed young Jupiter-sized planets to determine whether they are bonafide Jupiter-mass objects or puffy low-mass objects. In Section 3.1, we describe our target list of young planets and the selection criteria we use to build our list. The interior structure model we adopt to identify a plausible mass range for each planet in our sample is detailed in Section 3.2. Often, our interior models converge onto two *families* of solution, one at the lower mass end and the other at the higher mass end. In Section 3.3, we describe how we rule out the high mass family of solutions by comparing to the brown dwarf mass-radius-age curves. We further narrow the range of plausible mass in our low mass family of solution by constraining its lower limit against photoevaporative mass loss, as described in Section 3.4, and its upper limit against the known planetary and stellar metallicity trends, as described in Section 3.5.

3.1 Target Selection

We select confirmed planets younger than 1 Gyr with radii larger than $3R_\oplus$ from the NASA Exoplanet Archive (2023a,b), hereafter 'Archive'. Obtaining stellar age estimates can be a challenging and sometimes unreliable task. For the planets in our sample, we verified that all age estimates remained below 1 Gyr within the 1-σ uncertainty provided on the Archive. Only two of the oldest stars in our population, TOI-4087 and TOI-2152 A, which are hosts to confirmed hot Jupiters, fell well outside 1 Gyr. For both systems, the age estimates are obtained using EXOFASTv2 global fits, a code designed to fit exoplanet transit and radial velocity data and extract system parameters, such as stellar age, using a Markov Chain Monte Carlo method (Eastman et al., 2013, 2019). Since these planets are not the youngest in our study and already have mass measurements, they are not critical for our analysis. We nonetheless include them, since it is still interesting to verify our methods against these known hot Jupiters. For the rest of the planets, the uncertainty in their age is small enough that we can consider the estimates reliable for our purposes. The stars for which it is most important to have a reliable age estimate are the youngest in our study, most notably V1298 Tau, HIP 67522, and TOI-837. These young stars all belong to young clusters with known ages, and since stars in a cluster form together, this is a robust way of constraining stellar age. To constrain the cluster as a whole, an estimate is obtained from the ages of stars within the association. The ages of these stars can be obtained via methods such as stellar rotation measurements, where the rotation period of a star increases with age due to changes in the star's moment of inertia and angular momentum loss (see, e.g., Schatzman, 1962; Skumanich, 1972; Kawaler, 1988), and lithium line measurements, where lithium content decreases with time since stars destroy it via proton capture (see, e.g., Skumanich, 1972; Duncan, 1981). V1298 Tau, part of the stellar association Group 29, also has lithium content and rotational period measurements that confirm and further constrain the stellar age. For HIP 67522, part of the Scorpius-Centaurus OB association, the effective temperature and luminosity of the star are fit to stellar isochrones PARSEC 1.2 s (Bressan et al., 2012) and BHAC15 (Baraffe et al., 2015) to determine the stellar age and mass. The age estimate for TOI-837, part of the open cluster IC 2602, is taken to be an absolute range encompassing the results from age estimates obtained through different stellar isochrone fittings and lithium aging techniques (see Table 3 of Bouma et al., 2020). Therefore, we consider the ages of these stars to be reliable and continue with our analysis.

While we are primarily interested in Jupiter-sized planets, we extend our selection down to $3R_{\oplus}$ to verify the performance of our methods of estimating reasonable planetary masses. Some planets have multiple parameter sets available, so we prioritize data sets with planetary mass measurements and otherwise choose the default parameter from the Archive. We further require that all planets studied have the necessary information available to obtain incident bolometric flux values such as the bolometric luminosity of the host star and the planet's semi-major axis. If these two parameters are not available, then we estimate the stellar luminosity from the stellar effective temperature and radius using the Stephan-Boltzmann law. Likewise, we calculate the planet's semi-major axis from the orbital period and stellar mass using Kepler's law. We obtain an uncertainty on all flux values by propagating the errors on the measured values.

Based on our selection criteria, we retrieve 12 planets with known mass measurements and 14 planets either without a mass measurement or only with upper limits on their mass. The relevant planetary and stellar parameters of our selected planets are given in Tables 3.1 and 3.2, respectively. The final selection of planets is shown in Figure 3.1, where we indicate which of them fall in the hot or warm Jupiter regime based on their incident bolometric fluxes and radii. We consider potential gas giants as planets with $R_p \gtrsim 6R_\oplus$ and mark the distinction between hot and warm at an incident bolometric flux of $\sim 1.72 \times 10^8$ erg/s/cm^2, which corresponds to the incident flux from a sun-like star at a period of 10 days. We consider warm Jupiters to be planets with an incident bolometric flux between $\sim 1.72 \times 10^8$ erg/s/cm^2 and $\sim 3.17 \times 10^6$ erg/s/cm^2 (flux from a sun-like star at a period of 200 days). This figure shows that all but one of our larger planets have high enough incident fluxes that if massive enough, they would qualify as hot or warm Jupiters. TOI-1227 b (R$_p$ $\sim$ 9.572 R$_\oplus$) is the only planet in our sample with a flux that falls below the warm Jupiter regime, so this planet is not considered a hot or warm Jupiter candidate.

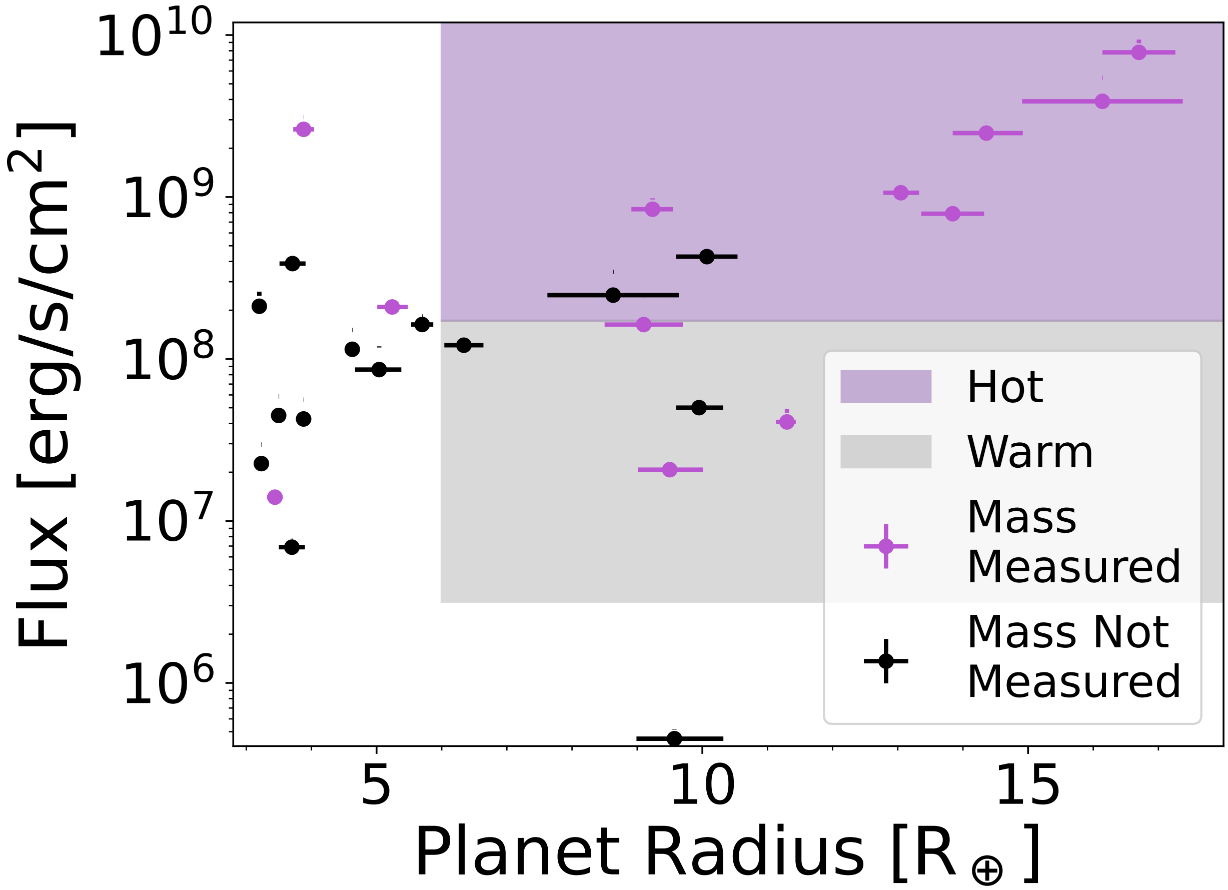

Figure 3.1: The incident bolometric fluxes and radii of the sample of planets studied in this work. The planets shown in purple have measured masses, while the ones shown in black do not. The grayed-out region indicates the planets that could potentially be warm Jupiters, while the purple region indicates those that could be hot Jupiters. We consider hot and warm Jupiters to be planets with an incident flux above that from a Sun-like star at a period of 10 days (F $\approx 1.72 \times 10^8$erg/s/cm^2, T$_{eq} \approx 1320$ K) and between 10 and 200 days (F $\approx 3.17 \times 10^6$erg/s/cm^2, T$_{eq} \approx 486$ K), respectively.

Planet	M_p [$M_\oplus$]	R_p [$R_\oplus$]	f_*† [erg/s/cm^2]	a [au]	P [days]	Reference
TOI-1268 b	$96.4^{+8.2}_{-8.3}$	$9.1^{+0.6}_{-0.6}$	$1.63^{+0.08}_{-0.09} \times 10^8$	0.0711	8.158	Šubjak et al. (2022)
TOI-1431 b	$991.62^{+57.21}_{-57.21}$	$16.70^{+0.56}_{-0.56}$	$7.82^{+0.16}_{-0.17} \times 10^9$	0.046	2.650	Addison et al. (2021)
TOI-2046 b	$731.01^{+88.99}_{-88.99}$	$16.14^{+1.23}_{-1.23}$	$3.90^{+0.15}_{-0.16} \times 10^9$	–	1.497	Kabáth et al. (2022)
TOI-4087 b	$232.01^{+44.50}_{-44.50}$	$13.05^{+0.28}_{-0.28}$	$1.06^{+0.01}_{-0.01} \times 10^9$	0.04469	3.177	Yee et al. (2023)
TOI-2152 A b	$899.45^{+120.77}_{-117.60}$	$14.36^{+0.56}_{-0.56}$	$2.48^{+0.04}_{-0.04} \times 10^9$	0.05064	3.377	Rodriguez et al. (2023)
TOI-201 b	$133.49^{+15.89}_{-9.53}$	$11.30^{+0.13}_{-0.01}$	$4.08^{+0.00}_{-0.00} \times 10^7$	0.3	52.978	Hobson et al. (2021)
TOI-622 b	$96.30^{+21.93}_{-22.88}$	$9.24^{+0.31}_{-0.31}$	$8.41^{+0.00}_{-0.00} \times 10^8$	0.0708	6.402	Psaridi et al. (2023)
V1298 Tau c	$19.8^{+9.3}_{-8.9}$	$5.24^{+0.24}_{-0.24}$	$2.09^{+0.00}_{-0.00} \times 10^8$	0.0839	8.249	Sikora et al. (2023)
V1298 Tau e	210^{+82}_{-82}	$9.5^{+0.51}_{-0.51}$	$2.07^{+0.00}_{-0.00} \times 10^7$	0.2667	46.768	Sikora et al. (2023)
HATS-36 b	$1022.14^{+19.71}_{-19.71}$	$13.84^{+0.48}_{-0.48}$	$7.89^{+0.08}_{-0.08} \times 10^8$	0.05425	4.175	Bayliss et al. (2018)
K2-25 b	$24.5^{+5.7}_{-5.2}$	$3.44^{+0.12}_{-0.12}$	$1.40^{+0.14}_{-0.13} \times 10^7$	0.0287	3.485	Stefansson et al. (2020)
K2-100 b	$21.80^{+6.20}_{-6.20}$	$3.88^{+0.16}_{-0.16}$	$2.62^{+0.05}_{-0.05} \times 10^9$	0.0301	1.674	Barragán et al. (2019)
TOI-1227 b	–	$9.572^{+0.751}_{-0.583}$	$4.53^{+0.62}_{-0.66} \times 10^5$	0.0886	27.364	Mann et al. (2022)
HIP 67522 b	–	$10.07^{+0.47}_{-0.47}$	$4.28^{+0.41}_{-0.42} \times 10^8$	–	6.960	Rizzuto et al. (2020)
TOI-837 b	< 381.396	$8.631^{+1.009}_{-1.009}$	$2.48^{+0.97}_{-0.97} \times 10^8$	–	8.325	Bouma et al. (2020)
DS Tuc A b	–	$5.7^{+0.17}_{-0.17}$	$1.63^{+0.20}_{-0.20} \times 10^8$	–	8.138	Newton et al. (2019)
HD 110082 b	–	$3.2^{+0.1}_{-0.1}$	$2.12^{+0.34}_{-0.49} \times 10^8$	0.113	10.183	Tofflemire et al. (2021)
TOI-2076 c	–	$3.497^{+0.043}_{-0.043}$	$4.48^{+0.14}_{-0.14} \times 10^7$	0.1093	21.015	Hedges et al. (2021)
TOI-2076 d	–	$3.232^{+0.063}_{-0.063}$	$2.26^{+0.70}_{-0.70} \times 10^7$	0.1539	35.125	Hedges et al. (2021)
HD 56414 b	–	$3.71^{+0.2}_{-0.2}$	$3.88^{+0.16}_{-0.16} \times 10^8$	0.229	29.050	Giacalone et al. (2022)
TOI-1136 d	–	$4.627^{+0.077}_{-0.072}$	$1.15^{+0.36}_{-0.36} \times 10^8$	–	12.519	Dai et al. (2023)
TOI-1136 f	–	$3.88^{+0.11}_{-0.11}$	$4.26^{+0.13}_{-0.13} \times 10^7$	–	26.316	Dai et al. (2023)
K2-33 b	< 1175.971	$5.04^{+0.34}_{-0.37}$	$8.60^{+0.32}_{-0.34} \times 10^7$	–	5.425	Mann et al. (2016)
V1298 Tau b	< 159	$9.95^{+0.37}_{-0.35}$	$5.01^{+0.53}_{-0.52} \times 10^7$	0.1716	24.140	Sikora et al. (2023)
V1298 Tau d	< 36	$6.34^{+0.3}_{-0.3}$	$1.22^{+0.13}_{-0.13} \times 10^8$	0.1101	12.402	Sikora et al. (2023)
K2-95 b	–	$3.7^{+0.2}_{-0.2}$	$6.89^{+0.70}_{-0.70} \times 10^6$	–	10.135	Mann et al. (2017)

Table 3.1: The mass (M_p), radius (R_p), incident flux (f_*), semi-major axis (a), and period (P) for the target planets in our study. All planetary parameters are obtained from the NASA Exoplanet Archive (2023a,b). Period values are rounded to 3 decimal places. † Calculated parameter, not obtained directly from the Archive.

Star	$\mathbf{Z}_*$ **[dex]**	$\mathbf{t}_*$ **[Gyr]**	$\mathbf{L}_*$ $[\log_{10}(L_\odot)]$	$\mathbf{T}_*$ **[K]**	$\mathbf{R}_*$ $[R_\odot]$	$\mathbf{M}_*$ $[M_\odot]$	**Stellar Type**
TOI-1268	$0.36^{+0.06}_{-0.06}$	$0.245^{+0.135}_{-0.135}$	–	5300^{+100}_{-100}	$0.92^{+0.06}_{-0.06}$	$0.96^{+0.04}_{-0.04}$	$K1-K2$
TOI-1431	$0.09^{+0.03}_{-0.03}$	$0.29^{+0.32}_{-0.19}$	$1.068^{+0.078}_{-0.047}$	7690^{+400}_{-250}	$1.92^{+0.07}_{-0.07}$	$1.90^{+0.10}_{-0.10}$	AmC
TOI-2046	$-0.06^{-0.15}_{-0.15}$	$0.45^{+0.43}_{-0.021}$	–	6250^{+140}_{-140}	$1.21^{+0.07}_{-0.07}$	$1.13^{+0.19}_{-0.19}$	$F8V$
TOI-4087	$0.237^{+0.079}_{-0.079}$	$0.8^{+1.2}_{-0.6}$	$0.176^{+0.025}_{-0.02}$	6060^{+74}_{-67}	$1.11^{+0.02}_{-0.02}$	$1.18^{+0.04}_{-0.04}$	–
TOI-2152 A	$0.282^{+0.075}_{-0.075}$	$0.83^{+1.1}_{-0.58}$	$0.653^{+0.069}_{-0.067}$	6630^{+300}_{-290}	$1.61^{+0.06}_{-0.06}$	$1.52^{+0.09}_{-0.09}$	$F4V$
TOI-201	$0.24^{+0.036}_{-0.036}$	$0.87^{+0.46}_{-0.49}$	$0.415^{+0.016}_{-0.017}$	6394^{+75}_{-75}	$1.32^{+0.01}_{-0.01}$	$1.32^{+0.03}_{-0.03}$	$F6V$
TOI-622	$0.09^{-0.07}_{-0.07}$	$0.9^{+0.2}_{-0.2}$	$0.474^{+0.010}_{-0.010}$	6400^{+100}_{-100}	$1.42^{+0.05}_{-0.05}$	$1.31^{+0.08}_{-0.08}$	$F6V$
V1298 Tau	$0.1^{+0.15\,\mathbf{(a)}}_{-0.15}$	$0.025^{+0.005}_{-0.005}$	–	5050^{+100}_{-100}	$1.355^{+0.03}_{-0.03}$	$1.157^{+0.06}_{-0.06}$	–
HATS-36	$0.28^{+0.037}_{-0.037}$	$0.62^{+0.55}_{-0.55}$	$0.215^{+0.043}_{-0.048}$	6149^{+76}_{-76}	$1.16^{+0.04}_{-0.04}$	$1.22^{+0.03}_{-0.03}$	$G0V$
K2-25	$0.15^{+0.03}_{-0.03}$	$0.73^{+0.05}_{-0.052}$	$-2.088^{+0.015}_{-0.016}$	3207^{+58}_{-58}	$0.29^{+0.01}_{-0.01}$	$0.26^{+0.01}_{-0.01}$	$M4.5V$
K2-100	$0.22^{+0.09}_{-0.09}$	$0.75^{+0.004}_{-0.007}$	–	5945^{+110}_{-110}	$1.24^{+0.05}_{-0.05}$	$1.15^{+0.05}_{-0.05}$	$G0V$
TOI-1227	–	$0.011^{+0.002}_{-0.002}$	$-2.6^{0.028}_{-0.03}$	3072^{74}_{-74}	$0.56^{0.03}_{-0.03}$	$0.17^{0.01}_{-0.01}$	$M4.5V-M5V$
HIP 67522	0	$0.017^{+0.002}_{-0.005}$	$0.243^{0.022}_{-0.023}$	5675^{75}_{-75}	$1.38^{0.06}_{-0.06}$	$1.22^{0.05}_{-0.05}$	–
TOI-837	$-0.069^{+0.042}_{-0.042}$	$0.035^{+0.011}_{-0.004}$	–	6047^{162}_{-162}	$1.02^{0.08}_{-0.08}$	$1.12^{0.06}_{-0.06}$	$G0/F9V$
DS Tuc A	$-0.080^{+0.060\,\mathbf{(b)}}_{0.060}$	$0.045^{+0.004}_{-0.007}$	$-0.14^{0.008}_{-0.008}$	5428^{80}_{-80}	$0.96^{0.03}_{-0.03}$	$1.01^{0.06}_{-0.06}$	$G6V$
HD 110082	$0.08^{0.05}_{-0.05}$	$0.25^{+0.05}_{-0.08}$	$0.281^{0.009}_{-0.009}$	6200^{100}_{-100}	$1.19^{0.06}_{-0.06}$	$1.21^{0.06}_{-0.06}$	$F8V$
TOI-2076	$-0.09^{0.04}_{-0.04}$	$0.34^{+0.08}_{-0.14}$	–	5200^{70}_{-70}	$0.77^{0.01}_{-0.01}$	$0.82^{0.04}_{-0.04}$	–
HD 56414	0	$0.42^{+0.14}_{-0.15}$	$1.158^{0.01}_{-0.01}$	8500^{150}_{-150}	$1.75^{0.07}_{-0.07}$	$1.89^{0.11}_{-0.11}$	–
TOI-1136	$0.07^{0.06}_{-0.06}$	$0.7^{+0.15}_{-0.001}$	–	5770^{50}_{-50}	$0.97^{0.04}_{-0.04}$	$1.02^{0.03}_{-0.03}$	–
K2-33	–	$0.009^{+0.001}_{-0.001}$	$-0.824^{0.079}_{-0.097}$	3540^{70}_{-70}	$1.05^{0.07}_{-0.07}$	$0.56^{0.09}_{-0.09}$	$M3.3$
K2-95	$0.14^{0.04}_{-0.04}$	$0.79^{+0.03}_{-0.03}$	$-1.635^{0.017}_{-0.017}$	3410^{65}_{-65}	$0.44^{0.02}_{-0.02}$	$0.43^{0.02}_{-0.02}$	–

Table 3.2: The stellar properties, including metallicity (Z_*), age (t_*), luminosity (L_*), effective temperature (T_*), radius (R_*), mass (M_*), and stellar type, for all the planet-hosting stars in our study. All stellar parameters are obtained from the NASA Exoplanet Archive (2023a,b), with individual references specified in Table 3.1. Metallicities for V1298 Tau (a) (Suárez Mascareño et al., 2021) and DS Tuc A (b) (Benatti et al., 2019) were obtained from the references indicated, since they were not available from the data source given in Table 3.1.

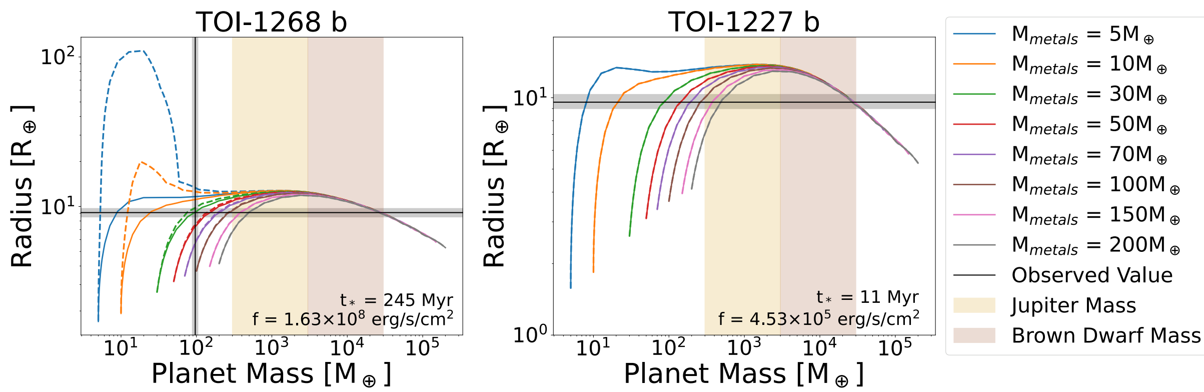

Figure 3.2: Left: Radius vs. mass for the age ($t_\star$) and incident flux (f) of TOI-1268 b. Each colour corresponds to varying metal masses with dashed lines vs. solid lines illustrating radius with and without extra heating (i.e. stellar heating) , respectively. The black lines and the surrounding grey zone show the measured radius and mass and their 1-σ error bar for this planet. The yellow-shaded region indicates the range of masses for a Jupiter mass planet, while the brown region indicates the range of masses for a brown dwarf. Our model produces a solution with a metal mass of $\sim 36.24 M_\oplus$ and a gas-to-metal mass ratio of ~ 1.66 for this planet, corresponding to the measured mass of 96.4 $M_\oplus$ and radius of 9.1 $R_\oplus$. Right: Same as the left panel , but for the planet TOI-1227 b, which does not have a measured mass. In this case, the incident flux is low enough that there is no noticeable difference from the extra heating. Using our model and additional mass loss and metallicity constraints (described in Sections 3.4 and 3.5), we obtain a final mass estimate ranging from $\sim 43.45 M_\oplus$ to $\sim 222.65 M_\oplus$.

3.2 Interior Structure Model

With the target list ready, we now use thermal evolution models from Thorngren et al. (2016) to constrain the mass of the planets given their radius, incident bolometric flux, and age. The thermal evolution of a planetary interior is constructed by solving the structure equations (hydrostatic equilibrium, mass conservation, and energy conservation, in that order):

$$\frac{\partial P}{\partial m} = -\frac{Gm}{4\pi r^2} \tag{3.1}$$

$$\frac{\partial r}{\partial m} = \frac{1}{4\pi r^2 \rho} \tag{3.2}$$

$$\frac{\partial L}{\partial m} = -T\frac{\partial S}{\partial T} \tag{3.3}$$

where P is pressure, m is mass, r is radius, ρ is density, L is luminosity, T is temperature, S is entropy, and G is the gravitational constant. We therefore solve for the radius-mass relationship for a given metal mass, gas-to-metal mass ratio, incident flux, and age. We make the distinction between core mass and metal mass (i.e. the total amount of metals in the planet) since not all heavy elements go into the planet's core. Giant planets require a ~ 10 $M_\oplus$ core to form, as described in Section 2.1.1, since runaway gas accretion typically occurs once the core has reached this critical mass. Furthermore, observational data indicate that sub-Neptunes have rocky cores with masses that can go up to ~ 20 $M_\oplus$ (Otegi et al., 2020). Therefore, if the planet is composed of less than or equal to 20 $M_\oplus$ of heavy elements, all metals go into the core and we consider a H/He envelope with solar metallicity. For planets with over 20 $M_\oplus$ of heavy elements, we put 20 $M_\oplus$ into the core and uniformly mix the remaining metals into the planet's H/He atmosphere using additive volumes. The final grid covers metal masses between 0.3 and 200 $M_\oplus$ in 60 logarithmic bins, gas-to-metal mass ratio between 10^{-6} and 10^3 in 33 logarithmic bins, incident fluxes between 10^4 and 10^{10} erg/s/cm^2 in 19 logarithmic bins, and ages from 10 Myr to 10 Gyr in 100 logarithmic bins.

Since many of our selected planets are under intense incident flux, we account for extra heating as described in Thorngren & Fortney (2018), where some of the irradiation from the star is being converted into heating the planet. In their models, Thorngren & Fortney (2018) assume that the heat is deposited into the interior adiabat. The effects of this extra heating are illustrated in Figure 3.2, for a planet with an incident flux of 1.68×10^8 erg/s/cm^2. When the incident flux is high, the extra heating effectively puffs up the planet, resulting in a larger radius for the same mass. This effect is more pronounced for smaller metal masses, since these planets have less heavy elements, the H/He envelope is more susceptible to expansion due to weaker gravitational potential. The right panel of Figure 3.2 shows a planet for which the incident flux is 4.53×10^5 erg/s/cm^2, which is low enough that the extra heating is negligible, so we see no difference between the two models.

Using the `RegularGridInterpolator` function from `scipy.interpolate` to interpolate between the grid points, we obtain the range of plausible total mass of a planet given their measured radius, incident flux, and age. [1] For each planet, we step through each of the 60 log-spaced metal mass grid points and use the `COBYLA` method of `scipy.optimize.minimize` to solve for the gas-to-metal mass ratio that produces a radius that matches the observed value within the tolerance of $10^{-5} R_{\oplus}$. Our models find two different solutions for each metal mass, one at low total mass (usually planetary) and another at high total mass (usually brown dwarf or stellar; see the right panel of Figure 3.2). For planets with mass measurements, the degeneracy between low and high total mass breaks (see the left panel of Figure 3.2).

When mass measurements exist, we solve for the unique metal mass and gas-to-metal mass ratios that agree with both the measured mass and radius. We also consider the edge cases, at the lower and upper limits given by the mass and radius error bars, and obtain 4 additional solutions at each of the bounds set by the measurement uncertainties. We then iterate through each of the 60 log-spaced metal masses from our grid. We check if there is a gas-to-metal mass or a range of gas-to-metal masses that produce a total mass and radius that fall within the bounds for the measured values. If there is, we solve for the gas-to-metal mass ratio at the bounds of the uncertainty. The number of solutions varies from planet to planet, depending on how many of the 60 metal masses have solutions that fall within the bounds of the measured mass and radius. Figure 3.3 shows the full set of solutions for

[1] We consider the incident flux to be constant for all stars in our sample. Since most stars are well past the pre-main sequence stage, which is a short timescale relative to their current age, assuming a constant luminosity has little effect. For the two stars that are still in the pre-main sequence stage (K2-33 and TOI-1227), we are probing them in a state of high luminosity. Furthermore, the radius dependence on incident flux is weak (Lopez & Fortney, 2014). Therefore, while assuming a constant flux is a source of uncertainty, it does not significantly affect our results.

a planet with a mass measurement, TOI-2046 b, which consists of the 5 solutions at the measured value and the uncertainty bounds, and 16 additional solutions which come from the 8 metal masses with gas-to-metal mass ratios that fall within the uncertainty region. The solutions show a range of metal masses and gas-to-metal mass ratios covering the limits given by the 1-σ uncertainty on the measured mass. We find that for all 12 planets in our study for which mass measurements are available, our model produces unique sets of solutions.

In the case where planets have a measured upper limit on their mass, we consider it as a hard cutoff for our mass range. In our sample, we have 4 such planets, TOI-837 b and K2-33 b with a 3-σ upper limit and V1298 Tau b and d with a 2-σ upper limit. Any solutions with total mass above this upper limit are discarded.

3.3 Ruling out the Brown Dwarf Solution

We now describe how we rule out the high-mass family of solutions for planets with no mass measurements. For the smaller planets in our sample (R $\lesssim$ 6 $R_\oplus$), we can rule out the high mass solution since it always falls beyond 100 M_J, well within the stellar mass regime. If these were stellar mass objects, given their radii ($\sim$ 3-10 $R_\oplus$), they would be dense enough to be considered compact objects. We therefore rule out these high mass solutions since it is unlikely that we are finding compact object companions. For the larger planets (R $\gtrsim$ 6 $R_\oplus$), we check the high-mass solution against predicted mass-radius curves at different ages for brown dwarfs from Baraffe et al. (2003). Figure 3.4 demonstrates how for all the large

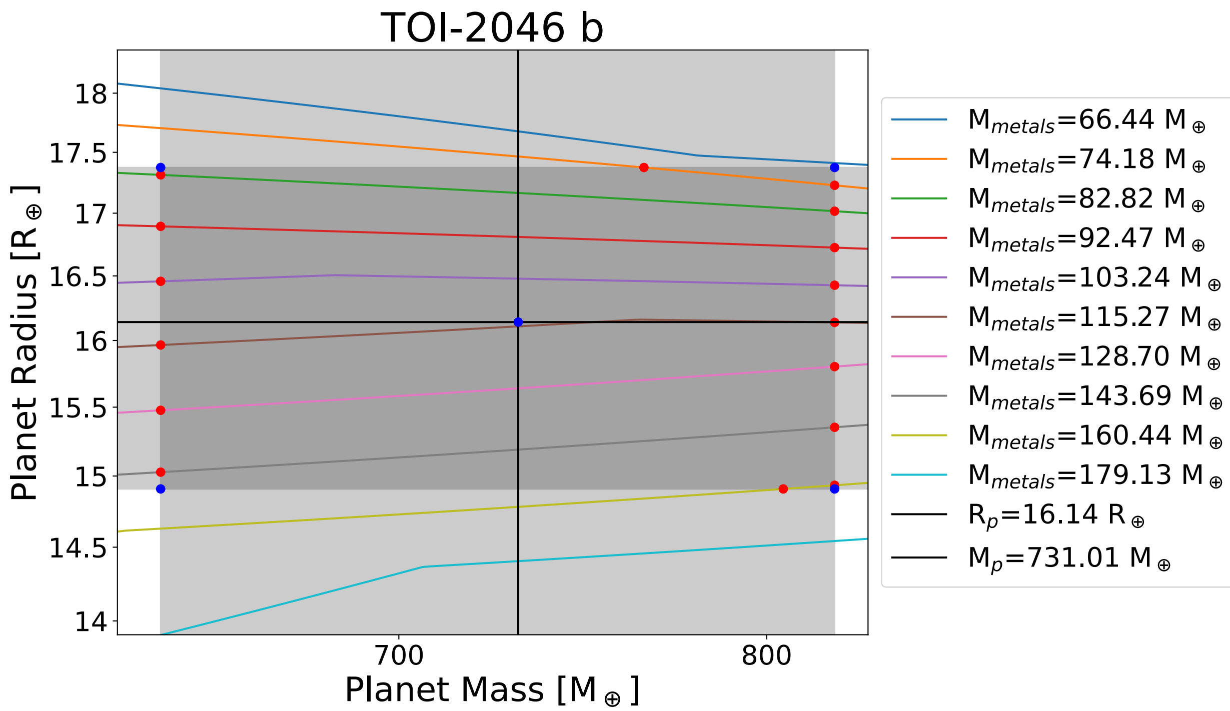

Figure 3.3: The metal mass and gas-to-metal mass ratio solutions for a planet with a mass measurement, TOI-2046 b. The measured mass ($M_p = 731.01 \pm 88.99 M_\oplus$) and radius ($R_p = 16.14 \pm 1.23 R_\oplus$) of the planet are shown as black lines, with their 1-σ error region shaded in grey. The metal mass and gas-to-metal mass ratio solutions at the measured radius and mass and the 4 bounds set by the measurement uncertainties are shown as blue circles. The coloured lines show the planet's mass and radius for 10 log-spaced metal masses between 66.44 $M_\oplus$ and 179.13 $M_\oplus$. Of those, 8 intersect the region bounded by the uncertainties in the measured radius and mass. An additional 16 metal mass and gas-to-metal mass ratio solutions at the points where those curves intersect the bounds are shown in red. For this planet, there is a total of 21 metal mass and gas-to-metal mass ratio solutions, which are checked against the mass loss and metallicity constraints described in Sections 3.4 and 3.5, respectively.

planets in our sample without mass measurements, their high-mass solutions either fall in the stellar mass regime or are too dense for their estimated ages ($\lesssim$ 35 Myr) and so we can safely rule such solutions out.

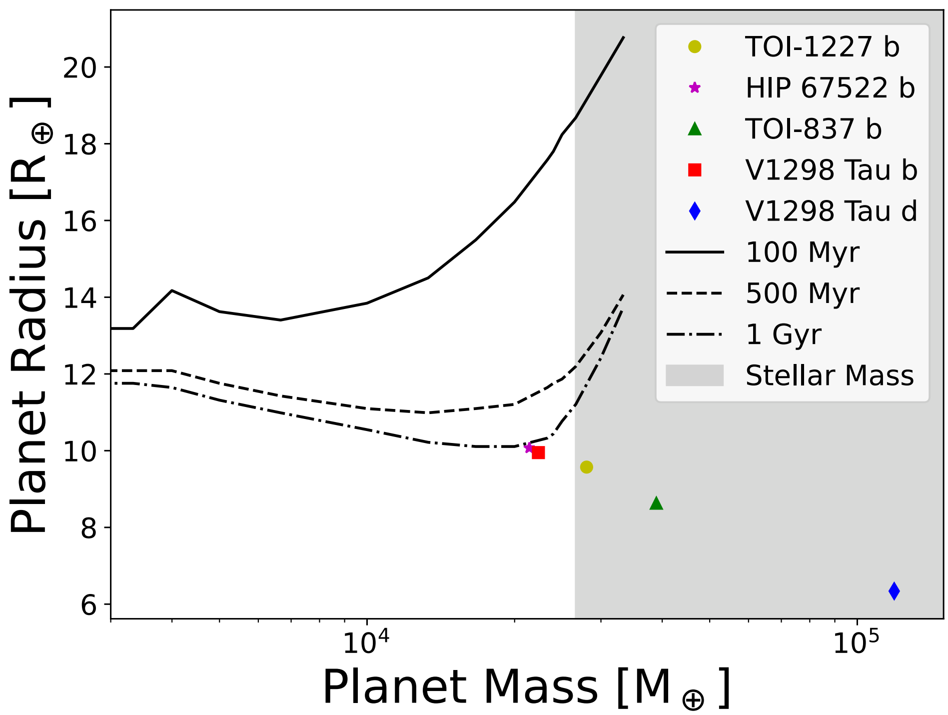

Figure 3.4: Verifying the validity of the high total mass solution. The black lines show the mass-radius relation at 100 Myr (solid), 500 Myr (dashed), and 1 Gyr (dot-dashed) (data obtained from Baraffe et al., 2003). The data points show the five planets in our sample without mass measurements with R $\gtrsim$ 6 R$_\oplus$. The grey region indicates the stellar mass range, where we can immediately rule out the solution for TOI-1227 b, TOI-837 b, and V1298 Tau d. Since all planets have ages less than 35 Myr, the grid solutions for HIP 67522 b and V1298 Tau b are much too dense to be brown dwarfs given the age of the planets. We therefore discard the high-mass solution for all planets in our sample.

3.4 Mass Loss

Now we describe how we place further mass constraints on the remaining low-mass family of solutions. We first consider photoevaporative mass loss to place a lower limit on the mass. Since most of our planets are large and heavily irradiated by their host stars, we use the empirical formula from Caldiroli et al. (2022), given by Equation 2.6, which encompasses both the energy-limited and the non-energy-limited regimes of atmospheric escape (see Section 2.2).

In Section 3.4.1, we discuss our choice and computation of f_{XUV}, comparing the methodologies presented in two papers, Johnstone et al. (2021) and King & Wheatley (2021), and ultimately choosing the latter. In Section 3.4.2, we examine a planet's stability against atmospheric escape by assessing whether the planet is able to hold on to the envelope mass inferred from presently measured properties over its age so that its final radius agrees with the observed radius within 1-σ error. In Section 3.4.3, we further examine the validity of a given solution by comparing its initial envelope pre-atmospheric escape against the formation model of Lee (2019). In some cases, a solution can survive the mass loss constraint in Section 3.4.2 but be ruled out by the Lee (2019) formation constraint in Section 3.4.3, so both constraints are necessary to determine the viability of a solution. We discuss in more detail and provide specific examples of planets for which this is the case in Section 3.4.3. Section 3.4.4 describes our runaway mass loss constraint, where we rule out solutions puffier than 0.1 g/cm^3 since such low-density planets would have likely undergone rapid atmospheric escape and lost their entire envelope (Thorngren et al., 2023). Planets without mass measurements are subject to all three mass loss constraints, while planets with mass measurements are only tested against the formation constraint in Section 3.4.3 and the runaway mass loss constraint in Section 3.4.4. Such a choice is made because we are guaranteed to lose the envelope mass solutions that are consistent with the lower bound of the 1-σ measurement error on radius for a given measured planet mass under the stability test in Section 3.4.2.

3.4.1 Comparing and Choosing a Source for the XUV Flux Evolution

To calculate mass loss, we need the time evolution of the XUV luminosity of the planet's host star over the lifetime of the system. We separately consider two stellar evolution grids which provide the bolometric luminosities throughout the star's lifetime, Johnstone et al. (2021) which provides grids for stars ranging from 0.1 to 1.2 $M_{\odot}$, and the MESA Isochrones & Stellar Tracks (MIST) (Dotter, 2016; Choi et al., 2016), which provides grids for stars with masses between 0.1 and 300 $M_{\odot}$ and metallicities from -4 to 0.5 dex.

First, we take the bolometric luminosity for a given stellar mass from the corresponding stellar evolution track. We note a slight discrepancy between the present-day measured values for the luminosity and the values from the stellar evolution grid at the age of the star.

To account for this, we use a scaling factor

$$f_* = \frac{L_{*,measured}}{L_{*,grid}(t_*)} \tag{3.4}$$

where $L_{*,measured}$ is the present-day measured luminosity and $L_{*,grid}(t_*)$ is the luminosity from the stellar evolution track at the stellar age. For each planetary system, we multiply the entire grid by this scaling factor so that the grid value at the age of the system matches the observed value. We then use the empirical relation to obtain the time-dependent X-ray luminosity:

$$L_X = \begin{cases} L_{sat} & t < 100Myr \\ L_{sat}\left(\frac{t}{100Myr}\right)^{-1.42} & t \geq 100Myr \end{cases} \tag{3.5}$$

where the value of the luminosity during the saturation interval is $L_{sat} = 10^{-3.6}L_*(t)$, $L_*(t)$ is the time-dependent bolometric luminosity over the lifetime of the star, and 100 Myr corresponds to a typical length for the saturation timescale. The power-law index describing the time dependence of X-ray luminosity is taken to be -1.42, which corresponds to the median value obtained by Tu et al. (2015) who use rotational evolution models to predict how stellar X-ray luminosity decays with time. Typically, this value is found to be between -1.5 and -1.2 (see, e.g., Jackson et al., 2012; Claire et al., 2012; Ribas et al., 2005). The EUV flux evaluated at the stellar surface, F_{EUV}, is then obtained from the following ratio:

$$\frac{F_{EUV}}{F_X} = \beta {F_X}^{\gamma} \tag{3.6}$$

where F_X is the X-ray flux evaluated at the surface of the star, γ is the power-law index and β is the scaling factor.

We compare the X-ray to EUV surface flux scaling equations from Johnstone et al. (2021) (hereafter J21) to the equations presented in King & Wheatley (2021) (hereafter KW21). Comparing the best-fit parameters from J21 and KW21, we find that the slopes and the general trends of the EUV flux as a function of X-ray flux are very different. KW21 generally find a steeper slope than J21, particularly in the soft EUV. KW21 also find that the hard EUVs (10-36 nm) and soft EUVs (36-92 nm) have a different slope (factor of ~2 difference), while J21 find that the two have similar slopes. In an attempt to better understand the equations presented in each paper and to get a better understanding of which of the two is more reliable, we attempt to reproduce the results of J21 and KW21 .

For our first check, we verify that the best-fit parameters presented in KW21 agree with the fits and data shown in their Figure 2, which shows the EUV to X-ray surface flux ratio. The best-fit parameters for the ratio of hard and soft EUV to X-ray surface flux given in the text are the power-law indices $\gamma_{hard} = -0.35^{+0.07}_{-0.15}$ and $\gamma_{soft} = -0.76^{+0.16}_{-0.04}$, with corresponding $\beta_{hard} = 116$ and $\beta_{soft} = 3040$. We find that using the best-fit parameters presented in the text of their paper does not reproduce the curves shown in their Figure 2. We conclude that this is due to a typo in the text of the paper, where β_{hard} should be 176 instead of 116. Using this corrected parameter, the equations match up with what is shown in their figure.

We perform a similar check on the J21 results and find that the X-ray to EUV surface flux ratio equations presented in the paper (their Equations 20 and 22) do not agree with their stellar evolution grids. Once again, we find that this is due to a typo in their paper, where they made a calculation error going from Equation 21 to Equation 22. The corrected parameters are $\gamma_{hard} = -0.319$ and $\gamma_{soft} = -0.373$ with $\beta_{hard} = 110$ and $\beta_{soft} = 34.4$.

Once these typos are corrected, we still notice a discrepancy between the results from the two papers. As a further check of both sets of results, we attempt to reproduce their main figures using the source data.

For KW21, we use TIMED/SEE data as described in their paper to obtain the results shown in their Figure 2.[2] We use the TIMED/SEE Solar Spectral Irradiance - Level 3 data from May 30th, 2002 to July 1st, 2014. The data contains the daily averaged solar irradiance spectra in 1 nm intervals at a distance of 1 AU (incident flux of the Earth). We consider wavelengths 0.5 to 9.5 nm for X-ray, 10.5 to 35.5 nm for hard EUV, and 36.5 to 91.5 nm for soft EUV and use `scipy.integrate.simpson` to integrate over the wavelength range to obtain the total incident flux. We then convert to stellar surface flux to match the data in KW21. Using `scipy.optimize.curvefit`, we fit Equation 3.6 to the TIMED/SEE data and obtain $\gamma_{hard} = -0.4039157 \pm 0.0000006$ and $\gamma_{soft} = -0.7551290 \pm 0.0000009$, with corresponding $\beta_{hard} = 270 \pm 4$ and $\beta_{soft} = 4000 \pm 1000$. The left panel of Figure 3.5 shows the

[2]The data used in KW21 is publicly available at `https://lasp.colorado.edu/see/data/daily-averages/level-3/`.

resulting TIMED/SEE data and fit we obtain compared to the results from KW21. We find that our analysis of the TIMED/SEE data does not produce the same best-fit parameters as obtained by KW21. However, the EUV fluxes obtained using our best-fit parameters differ by less than an order of magnitude from those obtained using KW21. We perform two independent mass loss calculations using each set of parameters and find that they produce almost the same final result. We see a difference in the final mass range for only 2 out of our 14 planets without mass measurements, TOI-1136 f and K2-95 b, where for each planet the calculation done with our fit parameters rules out one more solution than the calculation performed with the corrected fit parameters from KW21.

Therefore, given that our final results are not significantly affected by the difference in the parameters, we perform all calculations using the corrected best-fit parameters from KW21: the power-law indices $\gamma_{hard} = -0.35^{+0.07}_{-0.15}$ and $\gamma_{soft} = -0.76^{+0.16}_{-0.04}$, and corresponding $\beta_{hard} = 176$ and $\beta_{soft} = 3040$. We plan to further investigate the source of this disagreement in future work.

We perform a similar exercise on the J21 data. Their EUV fluxes are also obtained from solar data, using the Flare Irradiance Spectrum Model (FISM) (Chamberlin et al., 2007). Since FISM is not publicly available, we use the updated version of this model, FISM2 (Chamberlin et al., 2020). FISM2 is an improved, more reliable version of the original FISM, so we consider this a valid comparison to verify whether the parameters obtained by J21 match up with solar data. In their paper, J21 find that their models agree with the solar

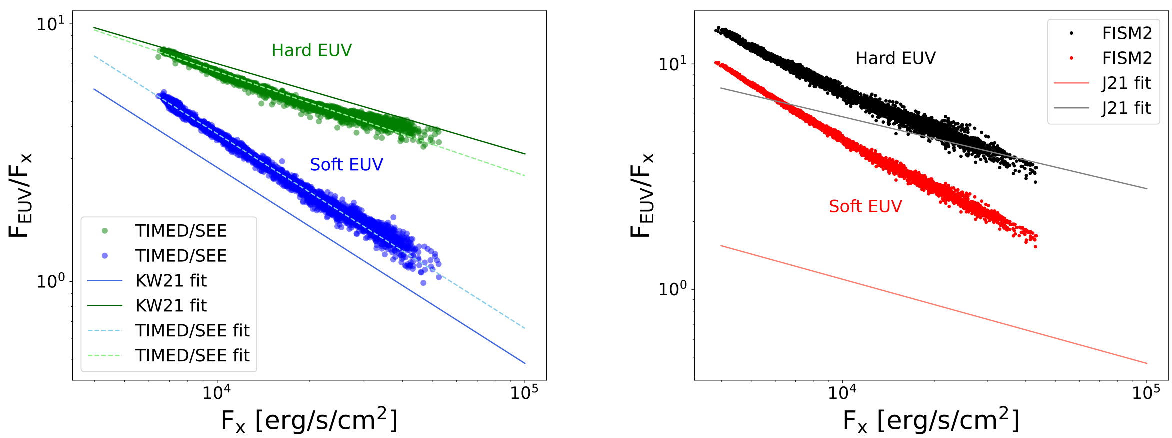

Figure 3.5: Left: The X-ray to EUV surface flux ratio for the solar data and scaling equations presented in King & Wheatley (2021). The TIMED/SEE solar data is shown as green and blue points, for hard and soft EUV, respectively. The dashed lines show the result of our power law fit, given by Equation 3.6, to the TIMED/SEE data. The solid lines show the ratio equations with the best-fit parameters from King & Wheatley (2021), corrected for the typo in the text (β_{hard} = 176, not 116). Right: Same as the left panel, using the equations and data presented in Johnstone et al. (2021). The black and red dots show the solar data from FISM2 (Chamberlin et al., 2020), for hard and soft EUV, respectively. The solid lines show the scaling relations presented in Equations 20 and 22 of Johnstone et al. (2021).

data from FISM. However, we find that FISM2 does not agree with the scaling relations presented in J21, particularly in the soft EUVs, where the EUV surface flux is almost an order of magnitude larger at low X-ray surface fluxes. The slopes of the FISM2 data are steeper (factor of two larger) than what is given by J21. The results of this exercise are shown in the right panel of Figure 3.5. We see that for both hard and soft EUV flux, the equations presented in J21 do not agree with the FISM2 data.

We conclude, given the discrepancy between the J21 equations and the FISM2 data that we cannot fully explain, that the J21 grid and scaling equations are not reliable enough for our purposes. Although we also find a slight disagreement between the TIMED/SEE data and the KW21 fit, the difference does not significantly affect our final results. Since our final mass ranges are robust to the difference in the EUV flux ratio fit parameters, we use the scaling equations from KW21 for all mass loss calculations. We also find that we are limited by the range of stellar masses for which stellar evolution tracks are available from J21 since some of our stars have masses larger than 1.2 $M_{\odot}$. Therefore, we use MIST instead of the J21 stellar evolution tracks. We perform all calculations using bolometric luminosities from MIST, Equation 3.5 to obtain the X-ray luminosity, and Equation 3.6 with the corrected best-fit parameters from KW21 to obtain the EUV surface fluxes. We then calculate the incident X-ray and EUV fluxes on the planet from the star and add them to obtain the incident high-energy flux, f_{XUV}.

3.4.2 Calculating Mass Loss

We obtain the XUV luminosity as described in Section 3.4.1. In our calculation, we use the equivalent evolutionary points (EEP) tracks for $v/v_{crit} = 0.4$ from MIST, for the measured stellar mass and metallicity rounded to the closest value for which a grid is available. For stars that do not have measured metallicities, we use a grid with solar metallicity.

For each metal mass, we solve for the gas-to-metal mass ratio given the radius, incident flux, and age of the planet, as described in Section 3.2. We consider this gas-to-metal mass ratio as the initial ratio and numerically integrate using the trapezoid method, going forward in time starting at 5 Myr. We take the timesteps from the MIST grid, which gives 454 log-spaced times from 0.032 yr to 1.806 Gyr, and slice the array to correspond to times 5 Myr $< t < t_*$. For the initial condition, we recalculate the radius of the planet given this gas-to-metal mass ratio at 5 Myr. At each iteration, we update the radius, mass, and incident flux, then the efficiency η and the reduction factor K. If we find that the entire envelope is lost, we end the calculation and consider the solution unstable to mass loss. Otherwise, we iterate until $t = t_*$, the stellar age, and check if the final radius after mass loss is within the error bounds of the observed radius. If it is, we consider the solution stable against mass loss, and otherwise, we rule it out. The left panel of Figure 3.6 shows the result of this test for V1298 Tau b, where all solutions with a final radius below the lower limit set by the 1-σ uncertainty on the measured radius are ruled out. We perform this calculation for each of the 60 metal mass and gas-to-metal mass ratio solutions obtained. This allows us to narrow down the mass range, constraining the lower limit, since solutions with small metal masses are particularly susceptible to atmospheric escape due to weak surface gravity.

3.4.3 'Backward' Mass Loss and Formation Constraint

Planets may very well have undergone significant mass loss in the early times so that their initial envelope mass is larger than that inferred from their present-day measurements. We therefore examine whether such an initial envelope is consistent with our fiducial formation model given by dusty accretion at close-in orbital periods presented in Lee (2019). We use a similar process as described in Section 3.4.2, except we begin at the stellar age, solve for the gas-to-metal mass ratio given the present-day parameters, and iterate backward in time up to 5 Myr, adding the amount of mass lost at each backward timestep, where we consider the same timesteps as in Section 3.4.2, to the current mass obtained from our radius grid. We repeat this calculation for each of the 60 metal masses in the radius grid, where we calculate the initial mass and radius of the planet for every solution obtained. Once the initial envelope mass is computed, we check the corresponding initial gas-to-metal mass and the metal mass against Figure 6 of Lee (2019). If our result lies above the maximum gas mass for the given metal mass, we rule out the solution. The result of this test for the planet V1298 Tau b is shown in the middle panel of Figure 3.6, where all solutions with gas mass above the limit set by Lee (2019) for a given metal mass are ruled out. A caveat to this test is that the maximum gas mass can be larger than what is presented in Figure 6 of Lee (2019) for subsolar metallicity gas and/or dust-free accretion (Lee & Chiang, 2015), which will be discussed in a case-by-case in Section 5.

It is possible for a solution to survive the mass loss constraint in Section 3.4.2 but be ruled out by the formation constraint from Lee (2019). Of the 14 planets without mass measurements, 4 have solutions that survive the mass loss but not the formation constraint. TOI-1227 b (radius $R=9.57R_{\oplus}$, incident bolometric flux $F=4.53\times10^{5}$ erg/s/cm^{2}) has 19 (lowest metal mass) out of 60 solutions ruled out by the formation constraint. In this case, the flux is so low that all solutions survive mass loss in Section 3.4.2, since there is almost no atmospheric escape. However, due to the large radius of the planet, many of the low metal-mass solutions are too puffy and gas-rich to be viable given the formation constraint from Lee (2019). In the case of V1298 Tau b ($R=9.95R_\oplus$, $F=5.01\times10^7$ erg/s/cm^2), which is shown in Figure 3.6, the 7 solutions with the smallest metal mass are ruled out by mass loss in Section 3.4.2 but the next 12 lowest metal mass solutions are still too puffy to survive the formation constraint. The same is true for K2-33 b ($R=5.04R_\oplus$, $F=8.60\times10^7$ erg/s/cm^2) and K2-95 b ($R=3.70R_\oplus$, $F=6.89\times10^6$ erg/s/cm^2), where the first 4 and 7 solutions, respectively, are ruled out by mass loss and the next 2 by formation.

We also perform this calculation on each of the solutions obtained for the planets with mass measurements. We use the same method as described above for each of the solutions to verify that they are stable against mass loss.

3.4.4 Runaway Mass Loss

We also check each of our solutions from the low-mass family of solutions against the runaway mass loss constraint from the bottom panel of Figure 1 from Thorngren et al. (2023). For each of the 60 solutions obtained, we verify whether the planet's bulk density is below 0.1 g/cm^3, the low-density boundary below which very few planets are seen in nature. Such planets would likely have undergone runaway mass loss, rapidly losing their entire envelopes.

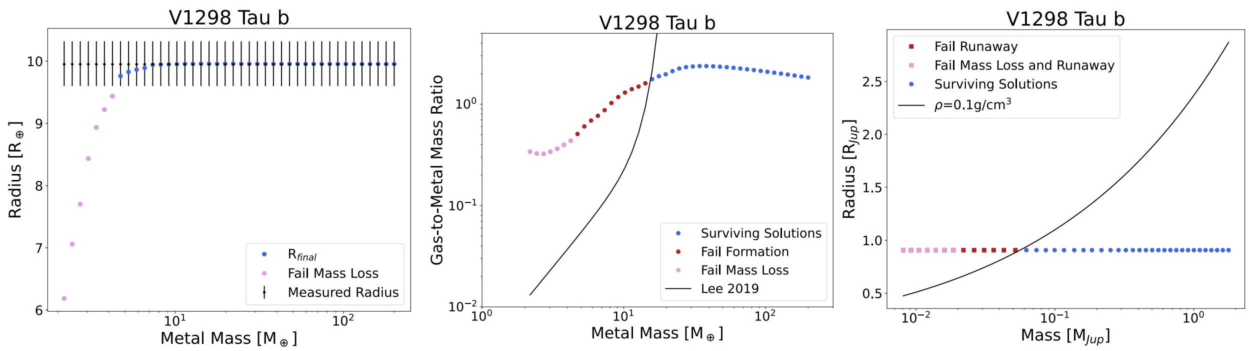

Figure 3.6: Ruling out solutions based on all three mass loss constraints described in Section 3.4 for a planet without a mass measurement, V1298 Tau b. Left: The result of the mass loss constraint, explained in Section 3.4.2. The black triangles show the measured radius, $R_p = 9.95R_\oplus$, with 1-σ error, while the circles show the final, post-mass loss radius. The solutions that fail this mass loss constraint are shown as purple circles, while the ones that survive are shown as blue circles. Middle: The result of the backward mass loss and formation constraint, described in Section 3.4.3. The black line shows the maximum gas mass that can be accreted for a given metal mass, from Lee (2019). Solutions above this line are ruled out by formation and are shown in red. Solutions that fail both the mass loss test (Section 3.4.2) and the formation test are shown in purple. The solutions that survive both tests are shown in blue. Right: The result of the runaway mass loss constraint, described in Section 3.4.4. The black line shows a bulk density of 1 g/cm^3. Solutions with bulk density puffier than this limit undergo runaway mass loss (Thorngren et al., 2023) and are ruled out. The squares show solutions that are ruled out by the runaway mass loss constraint, while the circles show solutions that survive. In this case, all solutions that fail the runaway mass loss test have already been ruled out by the mass loss constraint (shown in purple) or the formation constraint (shown in red). Solutions in blue survive all three mass loss constraints.

Any solutions puffier than this lower-density limit are considered unstable to mass loss and are discarded. The right panel of Figure 3.6 shows an example of this constraint applied to the solutions obtained for the planet V1298 Tau b. This same constraint is also applied to the solutions for the planets with mass measurements.

3.5 Planetary and Stellar Metallicity Constraints

For solutions with larger heavy element fractions, we consider planetary and stellar metallicity constraints. For each solution obtained, for all planets in our sample (with and without mass measurements), we check the metals-to-gas ratio against empirical mass-metallicity trends from Thorngren et al. (2016), which presents a study of the bulk compositions of transiting giant planets with masses $20M_{\oplus} < M_p < 20M_J$. We compare our results to the relationship they obtain between the planet's heavy element mass M_{met} and total mass M_p, given by

$$M_{met} = (57.9 \pm 7.03)M_p^{(0.61 \pm 0.08)}. \tag{3.7}$$

They further analyzed the correlation between the planet's bulk heavy-element enrichment and the host star's metallicity, finding

$$\frac{Z_p}{Z_{star}} = (9.7 \pm 1.28)M_p^{(-0.45 \pm 0.09)} \tag{3.8}$$

where Z_p=M_{met}/M_p is the planet metallicity and Z_{star} is the stellar metallicity. For each metal mass and gas-to-metal mass ratio solution, we verify whether the planet lies within the 1-σ region from the best fit. The intrinsic spread is given by $10^{\sigma} = 1.82 \pm 0.09$, so our 1-$\sigma$ region corresponds to the area within a factor of 1.82 from the best-fit line.

We consider these constraints only for solutions with total mass $M_p > 20M_{\oplus}$ since Thorngren et al. (2016) studied giant planets and their results do not extend to lower mass planets. We further limit our metallicity check on systems with measured host star metallicty so that in total, there are 22 planets eligible for our metallicity constraint analysis. An example is shown in Figure 3.7 which illustrates how the check on planet and stellar metallicity places an upper limit on the plausible planet and heavy element mass.

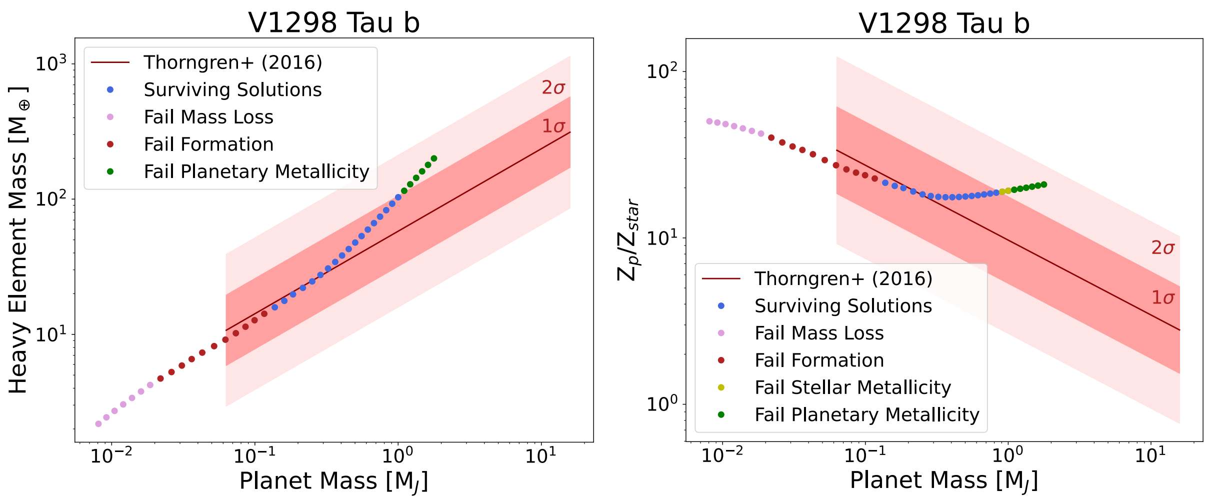

Figure 3.7: Ruling out solutions based on planetary and stellar metallicity constraints described in Section 3.5 for a planet without a mass measurement, V1298 Tau b. Left: Planetary metallicity trends from Thorngren et al. (2016). The best fit is shown as a red line, and the 1-σ and 2-σ regions are shaded in red. The solutions that fall outside the 1-σ region are ruled out and are shown in green. Solutions that fail the mass loss constraints in Section 3.4 are shown in purple (ruled out by mass loss, Section 3.4.2) and red (ruled out by formation, Section 3.4.3). The solutions in blue survive all constraints and make up the final mass range for the planet. Right: Same as the left, for the stellar metallicity constraint, based on the correlation between planetary and stellar metallicity and total planet mass from Thorngren et al. (2016). The solutions ruled out by this constraint are shown in yellow.

Chapter 4

Results

4.1 Planets With Mass Measurements

We successfully retrieve the metal mass and gas-to-metal mass ratio for all 12 planets with mass measurements. Metal mass and corresponding gas-to-metal mass solutions are obtained at the measured mass and radius, the 4 bounds of the uncertainties, and where any of the 60 log-spaced metal masses have metal-to-gas mass solutions that intersect the bounds set by the mass and radius measurement uncertainties. These solutions are subjected to the formation constraint (Section 3.4.3), the runaway mass loss constraint (Section 3.4.4), and the metallicity constraints (Section 3.5). Figure 4.1 shows the masses and radii of all planets with mass measurements, with errorbars colour mapped to the incident flux from the star and marker shapes and colours showing which planets survive the mass loss and metallicity tests. We find that all but one planet (K2-100 b) have all solutions stable to mass loss through the formation test described in Section 3.4.3. Figure 4.2 shows the result of the formation test on the solutions for the planet K2-100 b. Of the 15 solutions obtained for K2-100 b, 6 do not survive the formation constraint, including the 2 edge cases at the lower bound of the measured mass. All planets have all their solutions with bulk densities above 0.1 g/cm^3, so none fail the runaway mass loss test. When comparing the planetary and stellar metallicities to trends from Thorngren et al. (2016), as described in Section 3.5, we find that some solutions are outside the 1-σ range. While the 1-σ limit is a good reference, it is not unreasonable to find planets beyond that. We extend the constraint out to 2-σ and make note of the planets with solutions outside 1-σ for either of the metallicity trends. The results of the metallicity constraints are shown in Figure 4.3. Of the 12 planets with measured masses, 5 have all solutions within the 1-σ bounds of the best fit of both metallicity trends, and another 5 are within 2-σ. One planet, HATS-36 b, has some solutions that fall outside 2-σ for both metallicity constraints. TOI-201 b has all solutions well beyond 2-σ and is an outlier in our sample. We note that while the results from Thorngren et al. (2016) provide a good foundation for general metallicity trends, we cannot entirely disregard the possibility of outliers. Figures 7 and 11 of Thorngren et al. (2016) show the best-fit lines for the planetary and stellar metallicity trends, respectively, compared with the planets used to obtain the trends. Although most of the planets used to obtain the trends lie within the 1-σ region, a significant number have metallicities outside the 1-σ region. In each case, $\sim$40-50%

of the planets studied by Thorngren et al. (2016) lie outside the 1-σ region. Therefore, we can safely extend our constraint out to 2-σ without invalidating our results.

4.2 Planets Without Mass Measurements

Having shown that our methods can recover the measured mass for 11 of the 12 planets with mass measurements, given their measured radius, age, and incident flux, while satisfying all our constraints, we now move on to estimating the plausible mass range of the 14 planets without mass measurements. The final mass range obtained from our methods is shown in Figure 4.1, where the error bars without markers show the planets without mass measurements. We find that our method produces a solution which survives all constraints for 11 of the 14 planets studied, although in some cases, the final mass range is very narrow. We can obtain a mass range for the remaining 3 planets by loosening the metallicity constraint to rule out solutions outside the 2-σ region rather than the 1-σ region. Of all 14 planets, 10 fall well below the Jovian mass range ($M_p \lesssim 100 M_\oplus$), including two of our larger planets ($R_p > 6 R_\oplus$). The 4 remaining planets have part of their mass range falling in the gas giant planet regime. Of these 4, the one with the smallest radius ($\sim$4.6$R_\oplus$; TOI-1136 d) has solutions that just barely fall in the gas giant regime, with a maximum predicted mass of 106.58 M$_\oplus$. The other 3 planets (TOI-1227 b, V1298 Tau b, HIP 67522 b) are the largest in our study, with radii beyond 9 R$_\oplus$. It is important to note that TOI-1227 and HIP 67522 do not have stellar metallicity measurements, so the stellar metallicity constraint from Section 3.5 can not be used to test the upper limit on the mass. Obtaining metallicity measurements for these host stars could rule out some of the remaining high-mass solutions for their planets, further constraining the plausible mass range.

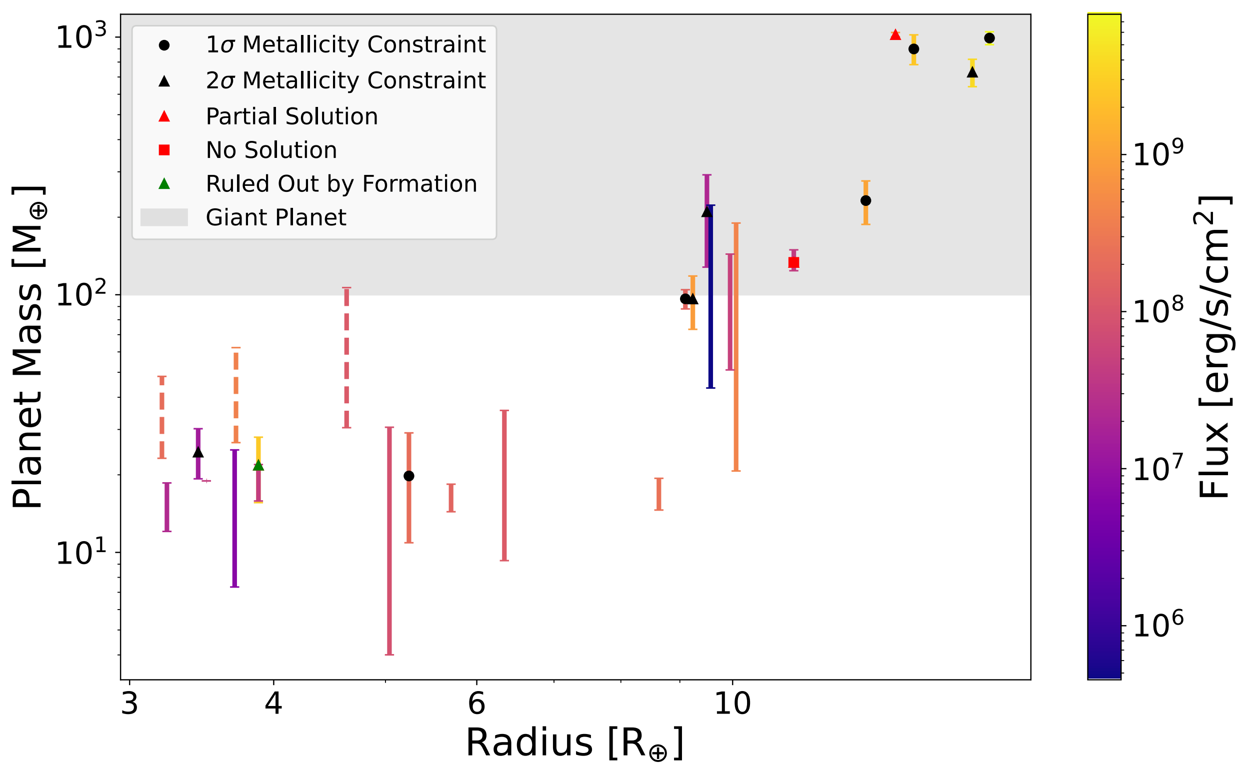

Figure 4.1: The total mass and radius of all 26 planets studied. All planets are shown with error bars color-mapped to their incident fluxes. The final mass ranges for the 14 planets without measured masses are shown by these error bars. Planets for which no solutions are found within 1-σ of the best-fit of the planetary and stellar metallicity trends from Thorngren et al. (2016), described in Section 3.5, are shown with dashed line errorbars. The 12 planets with mass measurements are shown with markers and error bars corresponding to the uncertainty of the measured mass. The black circles and triangles correspond to planets with all solutions within 1-σ and 2-σ, respectively, of the planetary and stellar metallicity trends from Thorngren et al. (2016). The red triangle (HATS-36 b) indicates that the planet has some solutions outside 2-σ, and the red square (TOI-201 b) indicates that all solutions fall outside 2-σ. We note that TOI-201 b is an outlier in our sample, being the only planet with all solutions outside 2-σ. The green triangle shows a planet (K2-100 b) for which some solutions fail the formation test described in Section 3.4.3 and all solutions are within the 2-σ region of the metallicity trends.

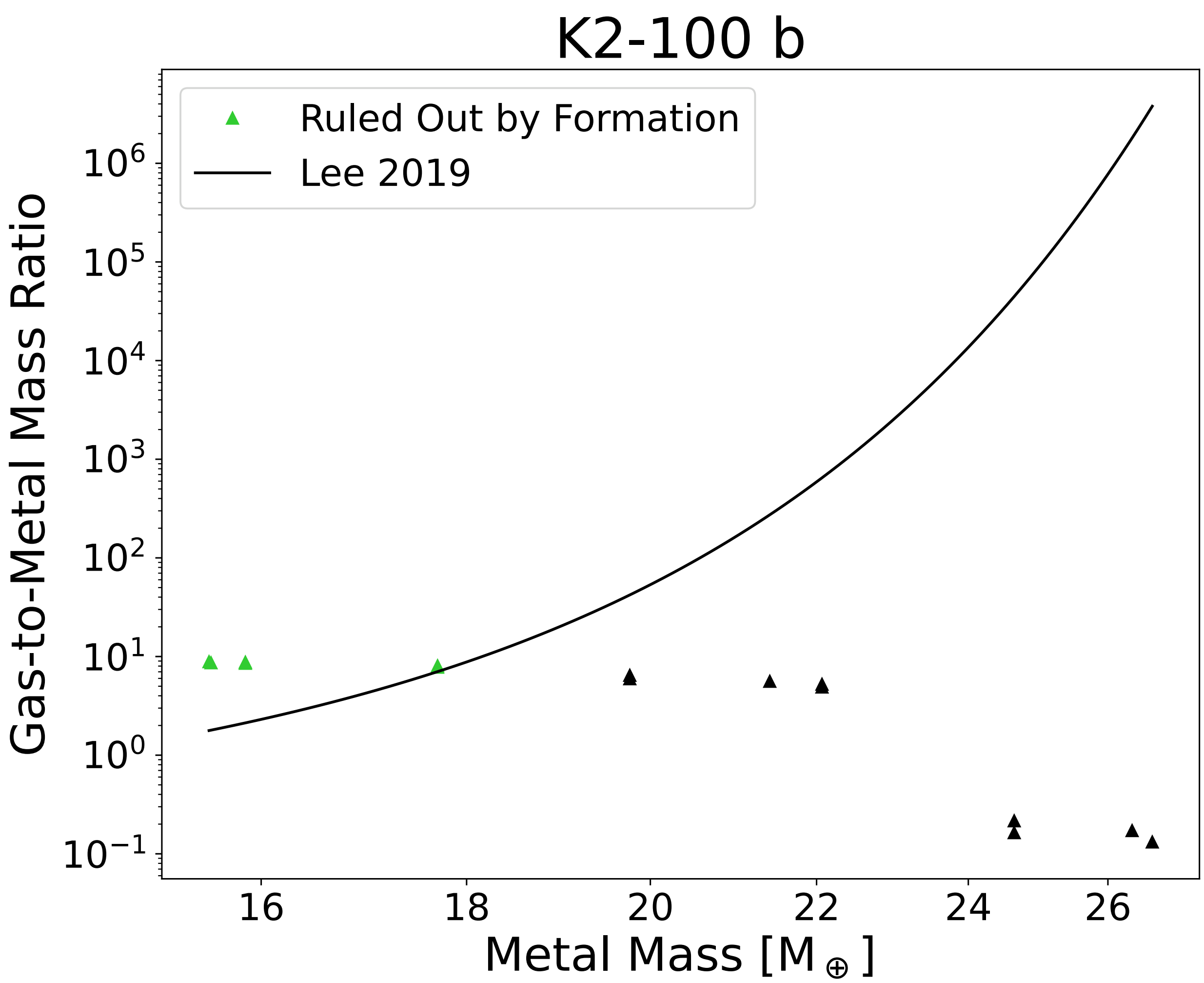

Figure 4.2: The result of the formation constraint on the planet K2-100 b, which has a measured mass of 21.80±6.20 $M_\oplus$ and radius of 3.88±0.16 $R_\oplus$. The solutions that do not survive the formation constraint from Lee (2019), described in Section 3.4.3, are shown in green, while the ones that do survive are shown in black.

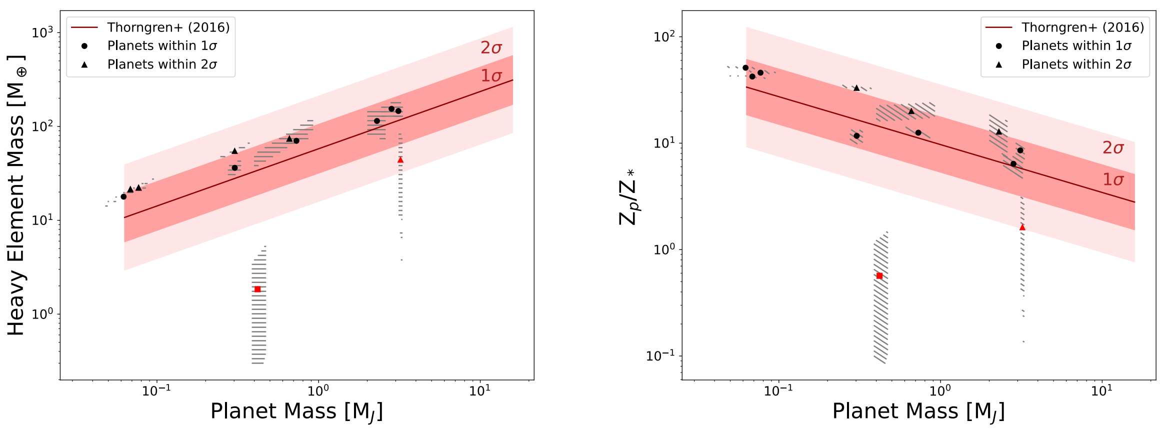

Figure 4.3: Comparing our planetary and stellar metallicities for the 12 planets with measured masses to the trends from Thorngren et al. (2016). Left: The planetary metallicity trend, where the relation of metal mass to total mass of the planet is compared to the best fit from Thorngren et al. (2016). The red-shaded regions show the posterior predictive 1-σ and 2-σ regions. The black circles correspond to planets with all solutions lying inside the 1-σ region. The black triangles correspond to planets with part or all of their solutions lying in the 2-σ region. The red triangle (HATS-36 b) and square (TOI-201 b) indicate that the planets have part and all of their solutions lying outside the 2-σ region, respectively. All planets are shown with grey hashed regions corresponding to the range of metal masses and total masses covered by the solutions that fall within the bounds set by the uncertainty on the measured mass and radius. Right: Same as the left panel, for the relation between the ratio of planetary to stellar metallicity and total mass.

Chapter 5

Discussion

We find that our constraints predict final masses well below the giant planet regime ($M_p \lesssim 50M_\oplus$) for the two smaller candidate hot Jupiters (V1298 Tau d, $R_p \sim 6.34R_\oplus$, and TOI-837 b, $R_p \sim 8.63R_\oplus$). For the three largest planets without mass measurements ($R_p \gtrsim 9\ R_\oplus$), we cannot rule out all solutions in the giant planet regime.

However, two of the three largest planets (HIP 67522 b, $R_p \sim 10.07R_\oplus$, and TOI-1227 b, $R_p \sim 9.57R_\oplus$) do not have stellar metallicity measurements, which removes one of the constraints on the upper limit on the mass. It is also important to note that TOI-1227 b is not considered a hot or warm Jupiter candidate due to its low incident bolometric flux ($f = 4.53\times10^5$ erg/s/cm^2). The stellar abundance can be an important constraint, particularly in the case where the star's metallicity is sub-solar. The predicted trends from Thorngren et al. (2016) find that metal-poor stars likely host metal-poor planets, a constraint which can significantly bring down the estimate for the upper limit of a planet's mass. TOI-837 b ($R_p \sim 8.63\ R_\oplus$) is an example of a planet whose host star's metal abundance places a strong constraint on the upper mass limit, where the mass estimated by our methods is $\lesssim 20\ M_\oplus$. Considering that the metallicity of the host star can provide a significant constraint on the mass of the planet, we emphasize the importance of following up on stellar abundances in the estimation of planet masses.

5.1 V1298 Tau b

Barat et al. (2023) studied the transmission spectrum of V1298 Tau b with the Hubble Space Telescope, from which they retrieved atmospheric properties which allowed them to constrain the planet's scale height. From this scale height, they were able to provide an upper limit on V1298 Tau b's mass, estimating $M_p = 24 \pm 5\ M_\oplus$. Our methods produce a final mass range for V1298 Tau b between $\sim$ 44 - 144 $M_\oplus$, which does not agree with the new measurement. Barat et al. (2023) find that the atmosphere of V1298 Tau b is metal depleted, with $Z = 10^{-0.1^{+0.66}_{-0.72}} Z_\odot$. Decreasing the atmospheric metallicity increases the boundary for the amount of gas that a given metal mass can accrete. A metal-depleted atmosphere has a lower opacity, which decreases the cooling timescale and allows for more gas accretion (see Section 2.1 for a review on planet formation). We modify Equation 5 from Lee (2019) to include the scaling factor for the atmospheric metallicity Z from Lee & Chiang (see 2015):

$$\frac{M_{gas}}{M_{metals}} = 0.09 \left(\frac{\Sigma_{neb}}{13g/cm^2}\right)^{0.12} \left(\frac{t}{0.1Myr}\right)^{0.4} \left(\frac{M_{metals}}{20M_\oplus}\right)^{1.7} \left(\frac{Z}{0.02}\right)^{-0.4} \times exp\left(\frac{t}{2.2Myr}\left(\frac{M_{metals}}{20M_\oplus}\right)^{4.2}\right) \quad (5.1)$$

where Σ_{neb}, the nebular gas surface density, is fixed to 13 g/cm^2, t, the accretion timescale, is fixed to 10 Myr, and 0.09 is the normalization factor from numerical calculations (Lee et al., 2014; Lee & Chiang, 2016). We find that to end up with a final mass $\sim$ 20-30 M$_\oplus$, V1298 Tau b's atmospheric metallicity must be less than $10^{-2.2}$Z$_\odot$ (Z$\lesssim$ 0.00013), which is $\sim$ 3-σ below the measured value presented in Barat et al. (2023). It is however possible that the interior metallicity of the atmosphere is different from the measured metallicity of the upper atmosphere (see Müller & Helled, 2024), which could account for the metal depletion required for the formation of such a puffy planet. The left panel of Figure 5.1 shows the formation constraint for the metal-depleted atmosphere compared to solar metallicity, where the former allows us to recover solutions with masses in agreement with the mass estimate from Barat et al. (2023).

The formation constraint described in Section 3.4.3 is for a dusty accretion disk, where metals in the disk contribute to the overall opacity in the form of dust grains. To have formed V1298 Tau b with a mass of $\sim$20-30 M$_\oplus$ in a dusty disk, its atmosphere must be significantly more metal depleted than what is measured by Barat et al. (2023), which is unlikely. Therefore, we also consider the formation of V1298 Tau b in a dust-free disk, where the dust grains do not contribute to the overall opacity of the disk, and adjust our equations accordingly based on the scaling from Lee et al. (2022), which includes a factor for disk temperatures T_d:

$$\frac{M_{gas}}{M_{metals}} = 3 \times 0.09 \left(\frac{\Sigma_{neb}}{13g/cm^2}\right)^{0.12} \left(\frac{t}{0.1Myr}\right)^{0.4} \left(\frac{M_{metals}}{20M_\oplus}\right)^{1.7} \left(\frac{Z}{0.02}\right)^{-0.4} \left(\frac{T_d}{1000K}\right)^{-1.5} \times exp\left(\frac{t}{2.2Myr}\left(\frac{M_{metals}}{20M_\oplus}\right)^{4.2}\right) \quad (5.2)$$

where the factor of 3 comes from visual inspection of Figure 3 from Lee et al. (2022) and we fix the atmospheric metallicity to the measured value (Z=$10^{-0.1}$Z$_\odot$). We can retrieve the orbital distance a at which the planet would have formed based on the disk temperature using

$$T_d = 1000K \left(\frac{a}{0.1au}\right)^{-3/7} \quad (5.3)$$

(see Chiang & Goldreich, 1997). V1298 Tau b is observed at an orbital distance of a$\sim$0.17 au but would have had to form slightly farther out (a$\gtrsim$0.33 au) in a dust-free disk, and have undergone some small amount of inwards migration post-formation. The right panel of Figure 5.1 shows the comparison between the dusty and dust-free formation constraint, where the latter is adjusted to recover the solutions which agree with the Barat et al. (2023) mass estimate.

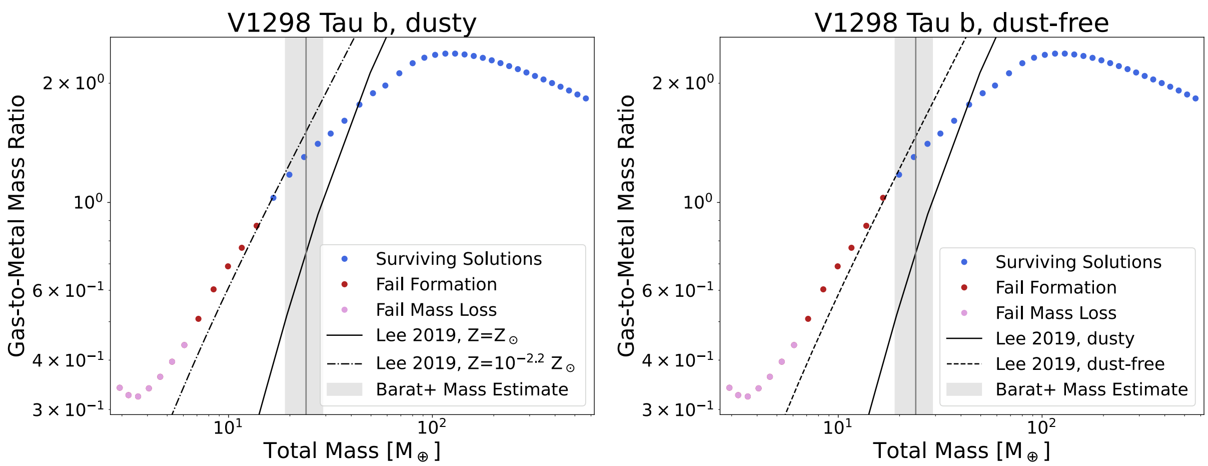

Figure 5.1: The results of adjusting the mass loss and formation constraint (described in Section 3.4.3) for the planet V1298 Tau b. The default constraint used in our methods is used to rule out all solutions too puffy to have formed (see the middle panel of Figure 3.6, where solutions to the left of the line are ruled out). We consider two ways of adjusting the constraint to recover solutions with masses corresponding to the new estimate from Barat et al. (2023), which both yield similar final results for the estimated mass range. Left: The formation constraint for a metal-depleted atmosphere. The dashed line and solid line show the maximum gas mass that can be accreted by a given metal mass for a subsolar ($Z=10^{-2.2}Z_\odot$) and solar atmospheric metallicity, respectively. Lowering the atmospheric metallicity from the default (solar) value used in our original methods (Section 3.4.3) allows us to recover the solutions in the estimated range from Barat et al. (2023) ($M_p=24\pm5M_\oplus$, shown in grey). Right: The formation constraint for a dust-free accretion disk, atmospheric metallicity from Barat et al. (2023) ($Z=10^{-0.1}Z_\odot$), at an orbital distance of $\sim$0.33 au, shown by the black dashed line. The default constraint described in Section 3.4.3 for dusty accretion, atmospheric metallicity $Z=Z_\odot$ and formation at 0.1 au is shown as a solid black line. In this case, the dashed line shows that we can recover the solutions that agree with the new mass estimate by considering formation in a dust-free disk (see Equation 5.2), slightly more far out than where it is observed (the observed orbital distance is $\sim$0.17 au).

5.2 HIP 67522 b

Recent atmospheric studies (Thao et al., 2024) have provided a new mass estimate for HIP 67522 b ($R_p \sim 10.07 R_\oplus$), predicting an upper limit of $\sim$20 $M_\oplus$. Our methods produce a final mass range with a lower limit $\sim$ 19.63 $M_\oplus$, which falls just below the new estimate. Figure 5.2 shows the results of the mass loss constraints, which affect the lower limit of our estimated mass range. Solutions between $\sim$ 14 $M_\oplus$ and $\sim$ 20 $M_\oplus$ are ruled out only by the runaway mass loss constraint, as shown in the right panel of Figure 5.2.

It is possible to recover the solutions down to a mass of $\sim$ 14 $M_\oplus$. Given the extremely young age of HIP 67522 b ($t_* \sim 17$ Myr), we may be observing the planet in a semi-runaway state, having not yet lost its entire envelope. Figure 5 of Thorngren et al. (2023) illustrates planets at various ages undergoing mass loss and thermal evolution and shows that at 10 Myr, small planets ($\sim$20 $M_\oplus$, $\sim$11 $R_\oplus$) have begun to lose mass but still have most of their envelopes. Our solutions between $\sim$ 14 $M_\oplus$ and $\sim$ 20 $M_\oplus$ are right below the runaway density limit of 0.1 g/cm^3, at a similar mass, radius and age to what is shown in Figure 5 of Thorngren et al. (2023). Therefore, we recover these solutions since such planets could still be observed before runaway mass loss has stripped them of their atmospheres.

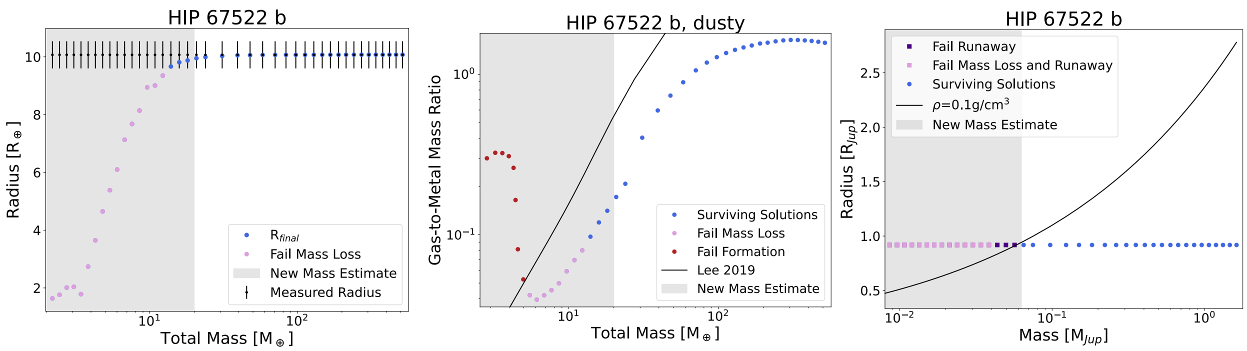

Figure 5.2: The results from the three mass loss constraints (described in Sections 3.4.2, 3.4.3, and 3.4.4, and shown in the left, middle, and right plots respectively) for the planet HIP 67522 b ($R_p \sim 10.07 R_\oplus$). We see that these constraints predict a final mass that is just barely in agreement with the upper mass limit (20 $M_\oplus$) from (Thao et al., 2024), shown as the gray region. However, given this planet's young age ($t_* \sim 17$ Myr), we can recover the 3 solutions ruled out only by runaway mass loss since it is likely that the planet is currently undergoing accelerated atmospheric escape but has not yet fully lost its envelope.

5.3 Implications for Hot Jupiter Migration

All the planets in our study with radii $\gtrsim 10$ $R_\oplus$ have mass measurements putting them well within the gas giant regime. These planets have ages ranging from $\sim$ 245 to 900 Myr, as shown in Figure 5.3. Although short, these are timescales over which high eccentricity tidal migration can bring these planets in from far-out orbits, since this migration process can operate over a timescale of a few 100 Myr (see, e.g., dynamical simulations from Naoz et al., 2011).

As for the youngest large planets, which are all less than $\sim$ 35 Myrs old, we find that they are generally more likely to be puffed-up Neptunes (see Figure 5.3). TOI-837 b ($t_* \sim$

35 Myr, $R_p \sim 8.63R_\oplus$, $M_p \lesssim 20M_\oplus$) is a prime example of a candidate hot Jupiter that our methods instead predict is a young, Neptune-mass planet with an inflated atmosphere that is still cooling and contracting (however, see Barragán et al., 2024). In addition, two planets, V1298 Tau b ($t_* \sim 25$ Myr) and HIP 67522 b ($t_* \sim 17$ Myr), have mass estimates obtained through recent atmospheric studies (Barat et al., 2023; Thao et al., 2024) which put them both around Neptune mass (see Sections 5.1 and 5.2, for V1298 Tau b and HIP 67522 b, respectively). Therefore, we see that the youngest planets in our sample with large radii ($R \gtrsim 8R_\oplus$) tend to be puffy, Neptune mass planets.[1]

The fact that the Jupiter mass planets are all more than a few 100 Myr old while all the youngest planets tend be puffed-up Neptunes provides tentative evidence that the dominant origin channel for hot Jupiters is likely high eccentricity migration. If disk gas migration were dominant, we would find Jupiter mass planets around stars as young as ~ 10 Myr, but we instead find that the youngest hot Jupiter candidates are inflated lower mass planets. Although this does not entirely rule out the possibility of disk gas migration, it hints that high eccentricity migration is likely more common. This result is consistent with obliquity measurements from Spalding & Winn (2022), who find evidence that most hot Jupiters arrive late ($\gtrsim 100$ Myr) based on tidal theory and stellar evolution models.

[1]For each of these three very young planets, we investigated the methods used to obtain their ages. All three host stars are part of young stellar clusters, V1298 Tau is part of the Group 29 stellar association, HIP 67522 is part of the Scorpius-Centaurus OB association, and TOI-837 is part of the open cluster IC 2602. The ages of these stars are validated through different sources and methods (e. g., stellar isochrones, lithium content). We therefore consider these age estimates to be reliable, making our conclusions robust.

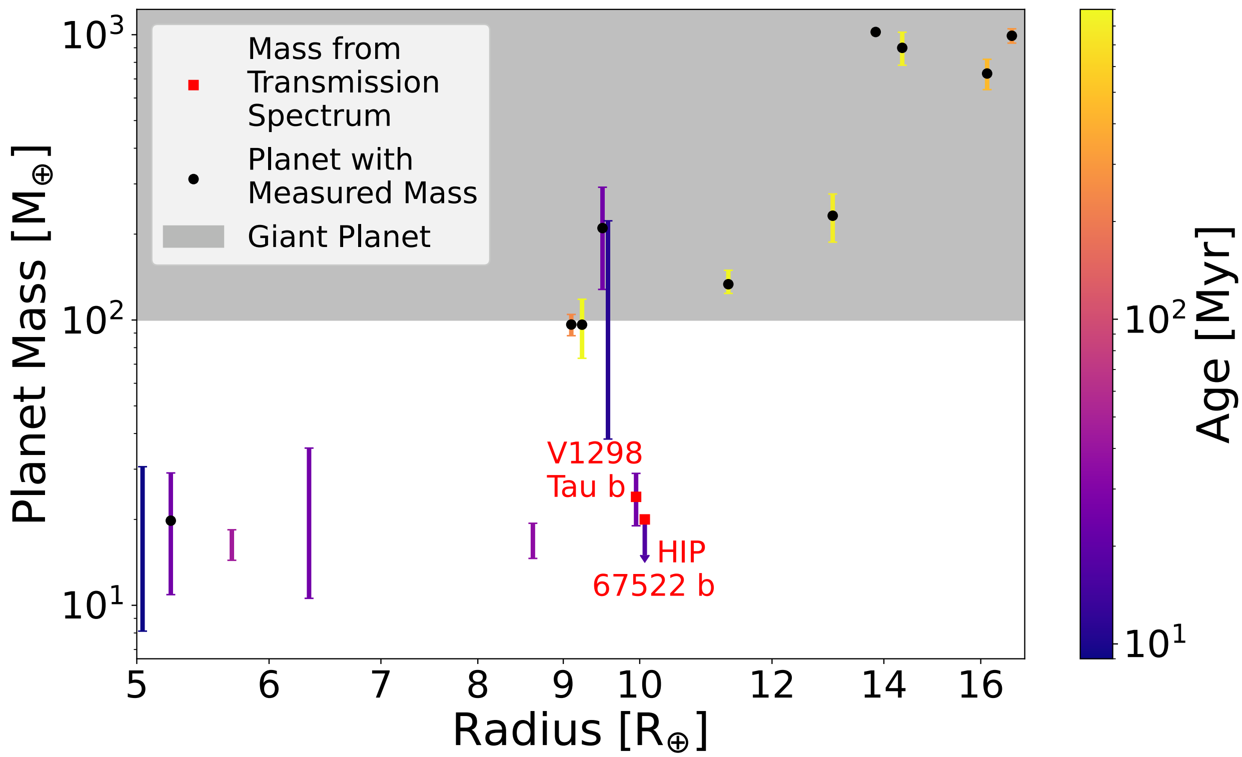

Figure 5.3: The final mass estimates for the larger planets studied ($R_p \gtrsim 5\ R_\oplus$), with error bars color mapped to the planet's age. The planets with mass measurements are shown with black circles. The two planets with recent mass estimates from atmospheric transmission spectra, V1298 Tau b and HIP 67522 b, are shown with red squares. HIP 67522 b only has an upper limit, denoted by an arrow. The planets without mass measurements do not have markers, and the error bar corresponds to the mass range predicted by our methods. The youngest planets ($\lesssim$ 100 Myr) tend to be lighter, Neptune mass planets, while the bonafide hot Jupiters are mostly found around older stars.

Chapter 6

Conclusion

In this thesis, we obtain a theoretical mass constraint on 26 young planets with ages ∼5-900 Myr and radii ∼3-16 $R_\oplus$ to determine whether they are massive hot Jupiters or merely puffy Neptunes. We use interior structure models to obtain an initial mass range which we narrow down using photoevaporative mass loss constraints and empirical mass-metallicity trends. For the candidate gas giants in our sample ($R_p \gtrsim 6R_\oplus$), our data and results show that planets with $R_p \lesssim 9R_\oplus$ all have final mass ranges placing them well below the gas giant regime. In contrast, for the largest planets ($R_p \gtrsim 9R_\oplus$), we cannot rule out all solutions in the giant planet regime. However, some of these largest planets do not have measurements for their host star's metallicity, which removes a constraint that can effectively limit a planet's maximum mass, particularly when hosted by a metal-poor star. Therefore, we emphasize the importance of following up on stellar abundances since they can effectively constrain the upper limit of a planet's estimated mass range. Furthermore, recent atmospheric studies have provided mass estimates $\sim 20\ M_\oplus$ for two of our largest planets, V1298 Tau b and HIP 67522 b, which agree with the results from our methods given adjustments for atmospheric metallicity, formation within a dusty vs. dust-free disk, or considerations of a planet in a semi-runaway state. We find that amongst the larger planets in our study ($R_p \gtrsim 6 R_\oplus$), those aged less than a few tens of Myr turn out to be puffy, lower-mass planets, while the bonafide hot Jupiters are only found around older stars, all aged more than a few hundred Myr. This suggests that hot Jupiters are likely not found around younger stars, which indicates that these gas giants likely migrate through a process that operates over longer timescales. Therefore, we can infer that the dominant migration mechanism for hot Jupiters is likely high eccentricity tidal migration.

Bibliography

Addison, B. C., Knudstrup, E., Wong, I., et al. 2021, AJ, 162, 292, doi: 10.3847/1538-3881/ac224e

Armitage, P. J. 2013, Astrophysics of Planet Formation (Cambridge University Press)

Baraffe, I., Chabrier, G., Barman, T. S., Allard, F., & Hauschildt, P. H. 2003, A&A, 402, 701, doi: 10.1051/0004-6361:20030252

Baraffe, I., Homeier, D., Allard, F., & Chabrier, G. 2015, A&A, 577, A42, doi: 10.1051/0004-6361/201425481

Barat, S., Désert, J.-M., Vazan, A., et al. 2023, Nature Astronomy. https://arxiv.org/abs/2312.16924

Barragán, O., Aigrain, S., Kubyshkina, D., et al. 2019, MNRAS, 490, 698, doi: 10.1093/mnras/stz2569

Barragán, O., Yu, H., Freckelton, A. V., et al. 2024, arXiv e-prints, arXiv:2404.13750, doi: 10.48550/arXiv.2404.13750

Batygin, K., Bodenheimer, P., & Laughlin, G. 2015, in AAS/Division for Extreme Solar Systems Abstracts, Vol. 47, AAS/Division for Extreme Solar Systems Abstracts, 300.06

Bayliss, D., Hartman, J. D., Zhou, G., et al. 2018, AJ, 155, 119, doi: 10.3847/1538-3881/aaa8e6

Benatti, S., Nardiello, D., Malavolta, L., et al. 2019, A&A, 630, A81, doi: 10.1051/0004-6361/201935598

Bondi, H. 1952, MNRAS, 112, 195, doi: 10.1093/mnras/112.2.195

Bouma, L. G., Hartman, J. D., Brahm, R., et al. 2020, AJ, 160, 239, doi: 10.3847/1538-3881/abb9ab

Bressan, A., Marigo, P., Girardi, L., et al. 2012, MNRAS, 427, 127, doi: 10.1111/j.1365-2966.2012.21948.x

Caldiroli, A., Haardt, F., Gallo, E., et al. 2022, A&A, 663, A122, doi: 10.1051/0004-6361/202142763

Chamberlin, P. C., Woods, T. N., & Eparvier, F. G. 2007, Space Weather, 5, S07005, doi: 10.1029/2007SW000316

Chamberlin, P. C., Eparvier, F. G., Knoer, V., et al. 2020, Space Weather, 18, e02588, doi: 10.1029/2020SW002588

Chiang, E. I., & Goldreich, P. 1997, ApJ, 490, 368, doi: 10.1086/304869

Choi, J., Dotter, A., Conroy, C., et al. 2016, ApJ, 823, 102, doi: 10.3847/0004-637X/823/2/102

Claire, M. W., Sheets, J., Cohen, M., et al. 2012, ApJ, 757, 95, doi: 10.1088/0004-637X/757/1/95

Dai, F., Masuda, K., Beard, C., et al. 2023, AJ, 165, 33, doi: 10.3847/1538-3881/aca327

Dawson, R. I., & Johnson, J. A. 2018, ARA&A, 56, 175, doi: 10.1146/annurev-astro-081817-051853

Dotter, A. 2016, ApJS, 222, 8, doi: 10.3847/0067-0049/222/1/8

Duncan, D. K. 1981, ApJ, 248, 651, doi: 10.1086/159190

Eastman, J., Gaudi, B. S., & Agol, E. 2013, PASP, 125, 83, doi: 10.1086/669497

Eastman, J. D., Rodriguez, J. E., Agol, E., et al. 2019, arXiv e-prints, arXiv:1907.09480, doi: 10.48550/arXiv.1907.09480

Erkaev, N. V., Kulikov, Y. N., Lammer, H., et al. 2007, A&A, 472, 329, doi: 10.1051/0004-6361:20066929

Ford, E. B., Kozinsky, B., & Rasio, F. A. 2000, ApJ, 535, 385, doi: 10.1086/308815

Giacalone, S., Dressing, C. D., García Muñoz, A., et al. 2022, ApJL, 935, L10, doi: 10.3847/2041-8213/ac80f4

Hedges, C., Hughes, A., Zhou, G., et al. 2021, AJ, 162, 54, doi: 10.3847/1538-3881/ac06cd

Hill, G. W. 1878, American Journal of Mathematics, 1, 5. http://www.jstor.org/stable/2369430

Hobson, M. J., Brahm, R., Jordán, A., et al. 2021, AJ, 161, 235, doi: 10.3847/1538-3881/abeaa1

Howell, S. B., Sobeck, C., Haas, M., et al. 2014, PASP, 126, 398, doi: 10.1086/676406

Ikoma, M., Nakazawa, K., & Emori, H. 2000, ApJ, 537, 1013, doi: 10.1086/309050

Inamdar, N. K., & Schlichting, H. E. 2016, ApJL, 817, L13, doi: 10.3847/2041-8205/817/2/L13

Jackson, A. P., Davis, T. A., & Wheatley, P. J. 2012, MNRAS, 422, 2024, doi: 10.1111/j.1365-2966.2012.20657.x

Johnstone, C. P., Bartel, M., & Güdel, M. 2021, A&A, 649, A96, doi: 10.1051/0004-6361/202038407

Kabáth, P., Chaturvedi, P., MacQueen, P. J., et al. 2022, MNRAS, 513, 5955, doi: 10.1093/mnras/stac1254

Kawaler, S. D. 1988, ApJ, 333, 236, doi: 10.1086/166740

King, G. W., & Wheatley, P. J. 2021, MNRAS, 501, L28, doi: 10.1093/mnrasl/slaa186

Lecavelier Des Etangs, A. 2007, A&A, 461, 1185, doi: 10.1051/0004-6361:20065014

Lee, E. J. 2019, ApJ, 878, 36, doi: 10.3847/1538-4357/ab1b40

Lee, E. J., & Chiang, E. 2015, ApJ, 811, 41, doi: 10.1088/0004-637X/811/1/41

—. 2016, ApJ, 817, 90, doi: 10.3847/0004-637X/817/2/90

Lee, E. J., Chiang, E., & Ormel, C. W. 2014, ApJ, 797, 95, doi: 10.1088/0004-637X/797/2/95

Lee, E. J., Karalis, A., & Thorngren, D. P. 2022, ApJ, 941, 186, doi: 10.3847/1538-4357/ac9c66

Lin, D. N. C., & Papaloizou, J. 1979, MNRAS, 186, 799, doi: 10.1093/mnras/186.4.799

—. 1986, ApJ, 309, 846, doi: 10.1086/164653

Lopez, E. D., & Fortney, J. J. 2014, ApJ, 792, 1, doi: 10.1088/0004-637X/792/1/1

Mamajek, E. E. 2009, in American Institute of Physics Conference Series, Vol. 1158, Exoplanets and Disks: Their Formation and Diversity, ed. T. Usuda, M. Tamura, & M. Ishii, 3–10, doi: 10.1063/1.3215910

Mann, A. W., Newton, E. R., Rizzuto, A. C., et al. 2016, AJ, 152, 61, doi: 10.3847/0004-6256/152/3/61

Mann, A. W., Gaidos, E., Vanderburg, A., et al. 2017, AJ, 153, 64, doi: 10.1088/1361-6528/aa5276

Mann, A. W., Wood, M. L., Schmidt, S. P., et al. 2022, AJ, 163, 156, doi: 10.3847/1538-3881/ac511d

Mayor, M., & Queloz, D. 1995, Nature, 378, 355, doi: 10.1038/378355a0

Michel, A., van der Marel, N., & Matthews, B. C. 2021, ApJ, 921, 72, doi: 10.3847/1538-4357/ac1bbb

Murray-Clay, R. A., Chiang, E. I., & Murray, N. 2009, ApJ, 693, 23, doi: 10.1088/0004-637X/693/1/23

Müller, S., & Helled, R. 2024, Can Jupiter's atmospheric metallicity be different from the deep interior? https://arxiv.org/abs/2403.16273

Naoz, S., Farr, W. M., Lithwick, Y., Rasio, F. A., & Teyssandier, J. 2011, Nature, 473, 187, doi: 10.1038/nature10076

NASA Exoplanet Archive. 2023a, Planetary Systems, Version: 2023-08-10 07:17:35, NExScI-Caltech/IPAC, doi: 10.26133/NEA12

—. 2023b, K2 Planets and Candidates Table, Version: 2023-08-10 07:17:35, NExScI-Caltech/IPAC, doi: 10.26133/NEA19

Newton, E. R., Mann, A. W., Tofflemire, B. M., et al. 2019, ApJL, 880, L17, doi: 10.3847/2041-8213/ab2988

Odert, P., Erkaev, N. V., Kislyakova, K. G., et al. 2020, A&A, 638, A49, doi: 10.1051/0004-6361/201834814

Otegi, J. F., Bouchy, F., & Helled, R. 2020, A&A, 634, A43, doi: 10.1051/0004-6361/201936482

Owen, J. E., & Jackson, A. P. 2012, MNRAS, 425, 2931, doi: 10.1111/j.1365-2966.2012.21481.x

Papaloizou, J. C. B., Nelson, R. P., Kley, W., Masset, F. S., & Artymowicz, P. 2007, in Protostars and Planets V, ed. B. Reipurth, D. Jewitt, & K. Keil, 655, doi: 10.48550/arXiv.astro-ph/0603196

Petrovich, C. 2015, ApJ, 805, 75, doi: 10.1088/0004-637X/805/1/75

Piso, A.-M. A., Youdin, A. N., & Murray-Clay, R. A. 2015, ApJ, 800, 82, doi: 10.1088/0004-637X/800/2/82

Pollack, J. B., Hubickyj, O., Bodenheimer, P., et al. 1996, Icarus, 124, 62, doi: 10.1006/icar.1996.0190

Psaridi, A., Bouchy, F., Lendl, M., et al. 2023, A&A, 675, A39, doi: 10.1051/0004-6361/202346406

Ribas, I., Guinan, E. F., Güdel, M., & Audard, M. 2005, ApJ, 622, 680, doi: 10.1086/427977

Ricker, G. R., Winn, J. N., Vanderspek, R., et al. 2015, Journal of Astronomical Telescopes, Instruments, and Systems, 1, 014003, doi: 10.1117/1.JATIS.1.1.014003

Rizzuto, A. C., Newton, E. R., Mann, A. W., et al. 2020, AJ, 160, 33, doi: 10.3847/1538-3881/ab94b7

Rodriguez, J. E., Quinn, S. N., Vanderburg, A., et al. 2023, MNRAS, 521, 2765, doi: 10.1093/mnras/stad595

Salz, M., Schneider, P. C., Czesla, S., & Schmitt, J. H. M. M. 2016, A&A, 585, L2, doi: 10.1051/0004-6361/201527042

Schatzman, E. 1962, Annales d'Astrophysique, 25, 18

Sikora, J., Rowe, J., Barat, S., et al. 2023, AJ, 165, 250, doi: 10.3847/1538-3881/acc865

Skumanich, A. 1972, ApJ, 171, 565, doi: 10.1086/151310

Spalding, C., & Winn, J. N. 2022, ApJ, 927, 22, doi: 10.3847/1538-4357/ac4993

Stefansson, G., Mahadevan, S., Maney, M., et al. 2020, AJ, 160, 192, doi: 10.3847/1538-3881/abb13a

Suárez Mascareño, A., Damasso, M., Lodieu, N., et al. 2021, Nature Astronomy, 6, 232, doi: 10.1038/s41550-021-01533-7

Thao, P. C., Feinstein, A., Mann, A., Gao, P., & Vanderburg, A. 2024, in AAS/Division for Extreme Solar Systems Abstracts, Vol. 56, AAS/Division for Extreme Solar Systems Abstracts, 201.03

Thorngren, D. P., & Fortney, J. J. 2018, AJ, 155, 214, doi: 10.3847/1538-3881/aaba13

Thorngren, D. P., Fortney, J. J., Murray-Clay, R. A., & Lopez, E. D. 2016, ApJ, 831, 64, doi: 10.3847/0004-637X/831/1/64

Thorngren, D. P., Lee, E. J., & Lopez, E. D. 2023, ApJL, 945, L36, doi: 10.3847/2041-8213/acbd35

Tofflemire, B. M., Rizzuto, A. C., Newton, E. R., et al. 2021, AJ, 161, 171, doi: 10.3847/1538-3881/abdf53

Tu, L., Johnstone, C. P., Güdel, M., & Lammer, H. 2015, A&A, 577, L3, doi: 10.1051/0004-6361/201526146

Šubjak, J., Endl, M., Chaturvedi, P., et al. 2022, A&A, 662, A107, doi: 10.1051/0004-6361/202142883

Ward, W. R. 1997, Icarus, 126, 261, doi: 10.1006/icar.1996.5647

Watson, A. J., Donahue, T. M., & Walker, J. C. G. 1981, Icarus, 48, 150, doi: 10.1016/0019-1035(81)90101-9

Wu, Y., & Murray, N. 2003, ApJ, 589, 605, doi: 10.1086/374598

Yee, S. W., Winn, J. N., Hartman, J. D., et al. 2023, ApJS, 265, 1, doi: 10.3847/1538-4365/aca286